

MEASUREMENT OF THE NEUTRON
PROTON SPIN CORRELATION
PARAMETER A_{zx}

INAUGURALDISSERTATION

zur Erlangung der Würde eines Doktors der Philosophie
vorgelegt der
Philosophisch-Naturwissenschaftlichen Fakultät
der Universität Basel

von

Markus Hauger

aus Basel BS

Basel 2002

Genehmigt von der Philosophisch-Naturwissenschaftlichen Fakultät
auf Antrag von Professor Dr. I. Sick und PD Dr. J. Jourdan.

Basel, den 3. Juli 2001

Prof. Dr. A. D. Zuberbühler
Dekan

Acknowledgements

I thank my advisors Ingo Sick and Jürg Jourdan for their steady support during my thesis. I thank for giving me the possibility to work on different experiments, which made the work varied and exciting.

I also want to thank all the former and actual members from our group, who helped setting up the experiment.

A special thank to our collaborators, the polarized target group from PSI, who made a great effort to develop the suitable polarized targets and operated the cryostat during the experiment.

Finally i thank the PSI crew, working hard to deliver a highly polarized and stable proton beam. Special thanks to Mr. Einken for the work on the polarized proton source and Mr. Schmelzbach for the beam setup.

Abstract

The n-p spin correlation parameter A_{zx} was measured at an energy of 66.24 MeV and 5 angles in the range of $25^\circ - 46^\circ$ CM with a statistical accuracy better than 0.01.

In the measured range, A_{zx} is most sensitive to ϵ_1 , the mixing parameter of the deuteron states 2S_1 and 2D_1 . Therefore the measurement is expected to reduce significantly the uncertainties of the phases in the energy range below 100 MeV, when a new global Phase Shift Analysis (PSA) is performed. This should help to find a more accurate answer to the strength of the tensor force in the NN-interaction.

The experiment was performed in the low energy area C (NEC) of the Paul Scherrer Institute (PSI) in Villigen, Switzerland.

Contents

Abstract	i
Contents	ii
List of Figures	iii
List of Tables	iv
1 Introduction	1
2 The Spin Correlation Parameter A_{zx}	4
2.1 The Coordinate Frame	4
2.2 Spin 1/2 Scattering	5
2.3 Definition of A_{zx}	8
2.4 Phase Shifts and Mixing Parameters	11
3 Experimental Setup	13
3.1 Scintillating Polarized Proton Target	14
3.2 Neutron Detector	16
4 Analysis	18
4.1 Beam Polarimeter	18
4.2 Electronic Setup	21
4.3 Determination Of The Sign Of The Neutron Beam Polarization	24
4.4 The Neutron Energy Distribution	26
4.5 The Effect Of The Target-Magnetic Field	30
4.6 Main Cuts	32
4.7 Normalization, Dead Time Correction and False Asymmetries .	34
4.8 The Carbon Background	38
5 Results	43
6 Discussion	45
7 Conclusion	47
A Neutron Spin Rotation in the FC-Magnetic Field	48
B Neutron Spin Rotation in the Target Field	50
C Error Calculations	51
D Asymmetry and Correction Factors	52

List of Figures

1	A_{zx} for different ϵ_1	2
2	ϵ_1 for different potentials and PSA	3
3	Coordinate Frame	4
4	Experimental Setup	13
5	Polarized proton target	14
6	Polarized target cryostat	15
7	Neutron Detector and Lead House	16
8	ADC spectrum from a PM of the neutron detector	17
9	Polarimeter electronics	19
10	Energy spectrum of the left Na-I	19
11	Polarization as a function of run numbers	21
12	Trigger electronics setup	23
13	n-p spin-transfer $K_x^{x'}$ and neutron energy distribution	26
14	Target time spectrum and simulation	27
15	Neutron polarization after the FC-field as a function of kinetic energy T	28
16	MC-simulated energy distribution from a 3 ns time target time cut	29
17	Target magnetic field	30
18	B_x and B_z as a function of the distance from the target	31
19	Polarizations of the beam at the target as a function of the incident energy	32
20	TOF versus Target time	33
21	TOF versus Target time (3 dimensional)	34
22	Target ADC spectra for the 5 neutron detector angles	35
23	TOF versus target time with a low energy cut in the target ADC	36
24	Pre-trigger to trigger asymmetry	37
25	FC asymmetry and $A_{ST/FC}$	38
26	Asymmetry from the background	39
27	Scattering from Carbon	40
28	TOF for neutron-carbon scattering and from n-p scattering	41
29	Carbon background	42
30	The present A_{zx} as a function of the CM-angle with different PSA interpolated values for ϵ_1	46
31	A_{zx} as a function of the energy	46
32	Scattering angle distribution in the lab frame for the 5 angles	51

List of Tables

1	Mean target polarization of the two experimental runs A_{zx} 99 and A_{zx} 00	15
2	Beam polarization of the experiment from the two run periods November '99 and March '00	21
3	Orientation of the proton spins after passing the Solenoid field	25
4	Spin-direction of the neutrons after the FC-field as a function of the initial proton polarization and the solenoid field direction .	25
5	A_y , A_{xx} , A_{yy} , A_{zz} and $ \epsilon_{\pm} $	43
6	Beam (P_b - and target- (P_t) polarizations and A_{zx} for different settings of the solenoid and the target polarization as a function of the target angles	44
7	A_{zx} at 66.24 MeV with the statistical error and systematical error	44
8	Systematic uncertainties	45
9	Measured asymmetries and correction factors	53

1 Introduction

The nucleon-nucleon (N-N) interaction at low energies can be described by the exchange of mesons [1]. In order to describe the N-N scattering data, potentials derived from meson theory contain the tensor force, which represents one of the most important parts. One of the characteristics of this force is the mixing of states with different angular momenta. The non vanishing deuteron quadrupole moment and the difference of the magnetic moment from $\mu_p + \mu_n$ were some of the earliest evidences for the existence of such a force in the N-N interaction [2]. Bethe [3] recognized that the tensor force gives the dominant contribution to the binding energy of the deuteron.

For 3- and 4-nucleon systems it is still an unanswered question, whether the binding energy can be understood in terms of a two-nucleon force (including the tensor force) or if in addition three-body forces contribute [1]. Calculations for the binding energy of 3H show that without a three-body force the measured binding energies can only be reproduced when the tensor force is weak [1, 4, 5].

A further consequence of the tensor force is the presence of the D-state in light nuclei. The exact contribution of mesonic degrees of freedom (meson exchange currents (MEC)) to the electromagnetic form factors of these nuclei can only be determined, when the contribution from the D-state is known [6], because the MEC and S-D transitions contribute with nearly equal size but with opposite sign to the form factors. For these reasons, it is necessary to measure the effects of the tensor force most accurately. One such measurement is presented in this work.

In a phase shift representation (PS) of the scattering data (see section 2.4 and [7, 8]) the mixing of different angular momenta is described by mixing parameters ϵ_J . The parameters describe mixing of states with $l \pm 1$ for given J , where J represents the total spin (angular momentum + spin). The mixing of such states is a direct consequence of the tensor force and therefore ϵ_J is a measure of its strength. Below 100 MeV the dominant mixing is the one between the lowest angular momenta $l = 0, 2$ described by the parameter ϵ_1 .

The measured quantity in this work, the neutron-proton spin correlation parameter A_{zx} , is most sensitive to ϵ_1 , the mixing parameter between the states 3S_1 and 3D_1 . On the other hand, it is insensitive to the phase 1P_1 , which is also poorly determined but in many observables strongly correlated with ϵ_1 . Figure 1 shows A_{zx} as a function of the center of mass (CM) scattering angle for different mixing parameters¹ ϵ_1 . Especially in the angular region where this experiment has been performed, A_{zx} shows a strong dependence on the mixing

¹The calculation is taken from a phase shift analysis from SAID (Scattering Analysis Interactive Dial-in) [9, 10], which is available via <http://gwdac.phys.gwu.edu>.

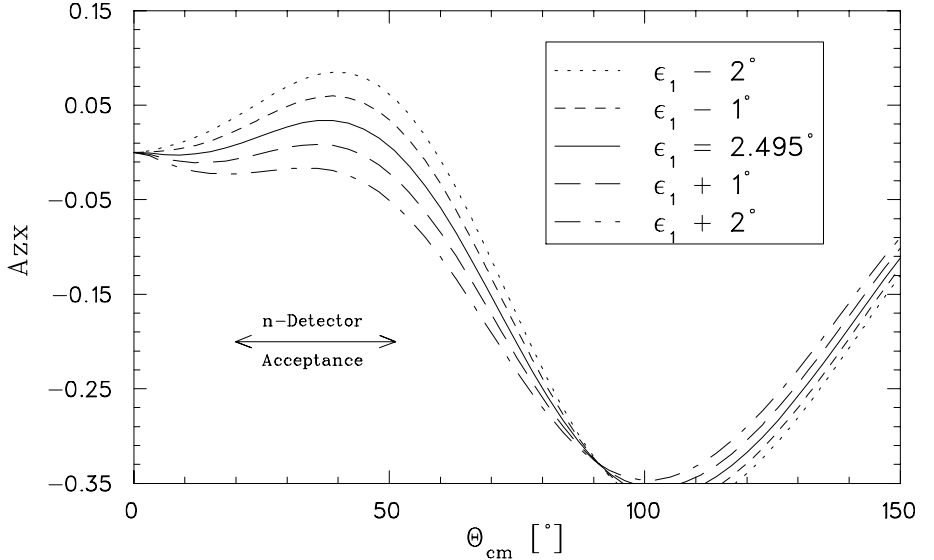


Figure 1: A_{zx} for different values of the spin correlation parameter ϵ_1 as a function of the CM scattering angle. Indicated is also the angular coverage of the present experiment.

parameter. In figure 2, ϵ_1 from different phase shift analyses (PSA) is plotted together with three theoretical potentials. The PSA seem to give higher values for ϵ_1 than the potentials predict, which is an indication for a stronger tensor force than given by present-day potentials.

The potentials have the following characteristics: The Paris potential [11] uses a dispersion theoretical approach starting with the knowledge of pion-nucleon phase shifts and pion-pion interaction for the medium and short range part down to 0.8 fm. Also 3π exchange is taken into account with a semi-phenomenological approach using the ω , a 3π resonance. The use of such resonances takes into account, that the exchange of correlated pions is more important than the exchange of uncorrelated ones. For the long range part the interaction is parameterized with the exchange of neutral and charged pions.

The Bonn potential [1] describes the interaction with a field theoretical approach for all distances. The one boson exchange is described using π , ρ and ω particles for long, intermediate and short interaction distances. The two pion contribution is treated in a fully quantum field theoretical way. In contrast to the Paris potential, the Δ isobar resonances of the nucleon and $\pi\pi$ correlations are also taken into account. The tensor coupling can mainly be explained using the vector-iso-vector meson ρ .

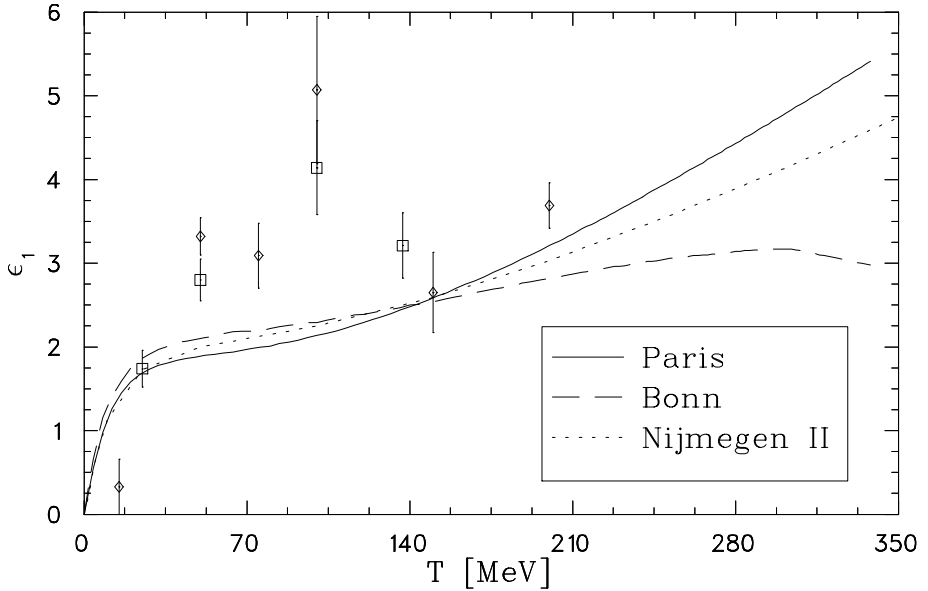


Figure 2: ϵ_1 as a function of the incident neutron kinetic energy for different potentials and PSA. The data points represent PSA from Henneck [5]: (\square) and Arndt [12]: (\circ)

The Nijmegen potential originates from a pure dispersion theoretical approach based on using information from N-N scattering (see reference [13]).

2 The Spin Correlation Parameter A_{zx}

The experiment measures an angle dependent asymmetry in the scattering of neutrons off protons. It will be shown that the measurement offers the possibility to learn about the spin dependent part of the neutron-proton interaction. For details see [14, 15]. The polarization of the proton target and the neutron beam are known as well as the energy distribution of the neutrons in the beam.

2.1 The Coordinate Frame

The definition of a coordinate frame is essential in polarization scattering experiments. Unfortunately there are many different conventions in literature and some leave still room for interpretation (See [16, 17, 15]).

In the present experiment all observables are related to the Bystricky-convention [18]. The nomenclature and coordinate frames defined in that article are unambiguous. The convention uses the same coordinates for the initially polarized beam and target. Nevertheless the observables and definition of the frame axis is done in the usual way, using x y and z , but in a way that it can be directly identified with the Bystricky-convention, namely $x \equiv s$, $y \equiv n$, $z \equiv k$.

The observables are all defined in the lab frame, nevertheless their dependence on kinematical variables like the momentum and the scattering angles can very well be described in the center of mass (CM) system. From the trans-

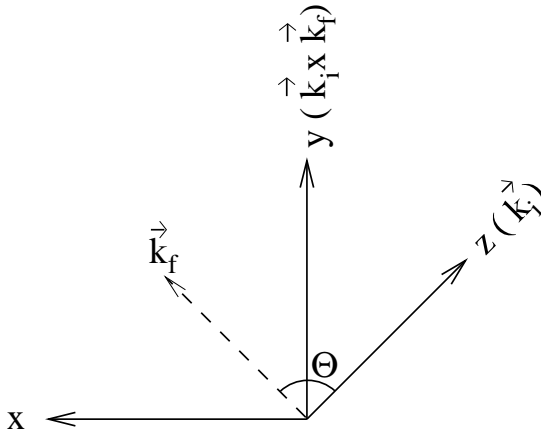


Figure 3: Coordinate Frame used in the present experiment. Note that the x and y axes are depending on the final momentum \vec{k}_f .

formation tables in [18] it is also easy to convert the observables themselves from the lab frame into the CM system.

The present frame is shown in figure 3: the z- axis is in direction of the incident beam momentum, the y-axis perpendicular to the initial and final momenta $\vec{k}_i \times \vec{k}_f$ of the neutrons and the x-axis forms a right handed system with \vec{e}_y and \vec{e}_z . Note that the x and y axis are depending on the final momenta. Hence each reaction has its own x and y axis.

2.2 Spin 1/2 Scattering

An arbitrary spin 1/2 one-particle state $|\Psi\rangle$ can be expressed with Pauli Spinors in momentum space as

$$|\Psi\rangle = \int \Psi^\uparrow(\vec{k}) |\vec{k}, \uparrow\rangle d^3k + \int \Psi^\downarrow(\vec{k}) |\vec{k}, \downarrow\rangle d^3k \quad (1)$$

$$:= \begin{pmatrix} \Psi^\uparrow(\vec{k}) \\ \Psi^\downarrow(\vec{k}) \end{pmatrix}. \quad (2)$$

$|\uparrow\rangle$ and $|\downarrow\rangle$ are states in \vec{e}_z , $-\vec{e}_z$ -direction respectively. The Hilbert space consisting in a beam and a target particle is

$$\mathcal{H} = (\mathcal{H}_b^{sp} \otimes \mathcal{H}_b^s) \otimes (\mathcal{H}_t^{sp} \otimes \mathcal{H}_t^s), \quad (3)$$

where H^s is the spin- and H^sp the spatial-part. This leads to a 2-particle state in \mathcal{H} :

$$|\Psi\rangle = |\psi\rangle_b \otimes |\psi_{in}\rangle_t = |\psi_b, \psi_t\rangle. \quad (4)$$

The derivation of the cross section is done in the center of mass frame. The initial momentum of the beam particle and the target in this frame are the same with opposite sign. The initial relative momentum shall be \vec{k}_i and the final momentum² \vec{k}_f . The system, consisting of a beam- and a target particle has a Hamiltonian of the form $H = H_0 + V = H_0^b + H_0^t + V$, where V is the interaction between the beam and the target in the center of mass frame. V is a potential acting on a free 2 particle state. In the unperturbed case (before scattering ($t \rightarrow -\infty$)) the system shall be in a pure eigenstate of the Hamiltonian H_0 (a plane wave with momentum \vec{k}_i):

$$|\Psi_i\rangle = |\psi_i\rangle_b \otimes |\psi_i\rangle_t = |\psi_i^b, \psi_i^t\rangle. \quad (5)$$

The propagation from the initial to final states is performed by a unitary time translation from $t = -\infty$ to $t = +\infty$, which leads to the propagator T:

$$T|\Psi_{in}\rangle = |\Psi_f\rangle \quad (6)$$

$$T := V + G_0 V + V G_0 V + G_0 V G_0 V + \dots \quad (7)$$

² \vec{k}_f is the direction of observation and not the final momentum of the scattered state unless when using the Born-approximation

T is expanded in a Dyson series with the interaction part of the Hamiltonian V and G_0 , the free Green's operator, which is the propagator without interaction [7]. Finally the differential cross³ section can be represented in terms of T or F, respectively:

$$\begin{aligned} d\sigma &= |\langle \Psi_f | F | \Psi_i \rangle|^2 \\ F &= c(\vec{k}) T. \end{aligned} \quad (8)$$

The difference of F and T is only a momentum dependent normalization factor c , usually $c = -(2\pi)^2/|\vec{k}|$.

Going to the real case, the target and the beam consist of a statistical ensemble of **incoherent** particles. Incoherence reduces the full Hilbert space to the one introduced in equation 3. The beam-target system in \mathcal{H} is best represented by a density operator ρ with the normalization $Tr\rho = 1$. The trace is taken over the spin and the momentum space. If there are N' protons in the target and N neutrons in the beam (per time interval), the full initial operator ρ_i can be written as

$$\rho_i = \rho_t \otimes \rho_b = \frac{1}{N N'} \sum_{m,n}^{N,N'} \sum_{s^1,s^2,s^3,s^4}^2 |b_m^{s^1}, t_n^{s^2}\rangle \langle t_n^{s^3}, b_m^{s^4}|. \quad (9)$$

The indices m and n are particle labels for the beam (b) and the target (t), respectively, and s^1 to s^4 are spin labels (\uparrow, \downarrow). Because ρ_t and ρ_b are one particle operators, the description applies to a two particle problem. The differential cross section for an ensemble is the same as in equation 8 but summed over all initial particles. In terms of the density operator, it is just the trace taken over the **final** density operator ($t \rightarrow +\infty$) in the spin space (Tr_Σ).

$$d\sigma = Tr_\Sigma [\rho_f]. \quad (10)$$

From the calculation of the full trace one would get the total cross section. In the spin-basis $\{|\uparrow\rangle_b |\uparrow\rangle_t, |\uparrow\rangle_b |\downarrow\rangle_t, |\downarrow\rangle_b |\uparrow\rangle_t, |\downarrow\rangle_b |\downarrow\rangle_t\}$, where the initial momentum defines the quantization axis (z-axis), ρ_i is a 4x4 Matrix with the coefficients:

$$\rho_i \hat{=} \frac{1}{N N'} \sum_{m,n}^{N,N'} \begin{pmatrix} |b_m^\uparrow(\vec{k}_i) t_n^\uparrow(-\vec{k}_i)|^2 & \cdots & |b_m^\downarrow(\vec{k}_i) t_n^\uparrow(-\vec{k}_i)|^2 \\ \vdots & \ddots & \vdots \\ |b_m^\uparrow(\vec{k}_i) t_n^\downarrow(-\vec{k}_i)|^2 & \cdots & |b_m^\downarrow(\vec{k}_i) t_n^\downarrow(-\vec{k}_i)|^2 \end{pmatrix}. \quad (11)$$

$b_m^\uparrow(\vec{k}_i)$ is a spinor in the beam and $t_n^\uparrow(-\vec{k}_i)$ one in the target space. The spinors are momentum dependent. But each particle in the beam or the target

³The differential cross section $\frac{d\sigma}{d\Omega}$ is written as $d\sigma$ for simplicity.

is assumed to be free and the cross section is derived for a **single momentum** ensemble. ρ_i can therefore be split into the spin and the momentum part, where the latter is just $\delta(\vec{k} - \vec{k}_i)$. Further $\hat{\rho}_i$ shall denote the density in the spin space and $\tilde{\rho}_i$ the density in the momentum space.

The initial polarizations of the beam and the target (\vec{P}_b and \vec{P}_t) are calculated from the expectation values of the usual Pauli matrices acting in the subspace of the beam and the target, respectively. They are known from the measurement of elastic $^{12}C(\vec{p}, p)$ -scattering and from the spin transfer in the $D(\vec{p}, \vec{n})pp$ -reaction (see section 4).

$$\vec{P}_b = \langle \vec{\sigma}_b \otimes 1_t \rangle_{\hat{\rho}_i} = Tr_{\Sigma} [\hat{\rho}_i (\vec{\sigma}_b \otimes 1_t)] \quad (12)$$

$$\vec{P}_t = \langle \vec{\sigma}_t \otimes 1_b \rangle_{\tilde{\rho}_i} = Tr_{\Sigma} [\tilde{\rho}_i (\vec{\sigma}_t \otimes 1_b)]. \quad (13)$$

For simplicity the unity operator 1 is omitted below, whenever it is obvious in which space the operators act. Building the trace in equation 12, 13 the polarization has the form

$$\vec{P}_b = \frac{1}{2N} \sum_{m=1}^N \begin{pmatrix} b_m^\dagger b_m^{\dagger*} + b_m^{\dagger*} b_m^\dagger \\ 2 \operatorname{Im} (b_m^\dagger b_m^{\dagger*}) \\ |b_m^\dagger|^2 - |b_m^{\dagger*}|^2 \end{pmatrix}. \quad (14)$$

Hence the initial density operator can be expressed in terms of the target and the beam polarizations:

$$\rho_i = 1/4 \tilde{\rho}_i (1 + \vec{P}_b \vec{\sigma}_b + \vec{P}_t \vec{\sigma}_t + \vec{P}_b \vec{\sigma}_b \otimes \vec{P}_t \vec{\sigma}_t). \quad (15)$$

The operator connecting initial and final states, introduced in equation 7, is again a 4x4 matrix in the basis chosen above:

$$F(\vec{k}, \vec{k}_f) := \begin{pmatrix} F_{\uparrow\uparrow}^{\uparrow\uparrow} & \dots & F_{\uparrow\uparrow}^{\downarrow\downarrow} \\ \vdots & \ddots & \vdots \\ F_{\downarrow\downarrow}^{\uparrow\uparrow} & \dots & F_{\downarrow\downarrow}^{\downarrow\downarrow} \end{pmatrix}. \quad (16)$$

The superscript arrows show the spin transfer of the beam particles, where the subscript arrows describe the spin transfer of the target. F is also depending on initial (\vec{k}) and final (\vec{k}_f) momenta. In this frame the final density operator can be written as

$$\rho_f = F \rho_i F^+. \quad (17)$$

ρ_f can again be expressed in terms of the initial polarizations as the initial density in equation 15:

$$\begin{aligned} \rho_f &= 1/4 (F \tilde{\rho}_i F^+ + F [\tilde{\rho}_i \vec{P}_b \vec{\sigma}_b] F^+ \\ &+ F [\tilde{\rho}_i \vec{P}_t \vec{\sigma}_t] F^+ + F [\tilde{\rho}_i \vec{P}_b \vec{\sigma}_b \otimes \vec{P}_t \vec{\sigma}_t] F^+). \end{aligned} \quad (18)$$

Since the polarizations are scalars and the initial momentum is fixed, the final density can be written as

$$\begin{aligned} \rho_f &= 1/4 (F \tilde{\rho}_i F^+ + \vec{P}_b F [\tilde{\rho}_i \vec{\sigma}_b] F^+ + \vec{P}_t F [\tilde{\rho}_i \vec{\sigma}_t] F^+ \\ &+ (\vec{P}_b F [\tilde{\rho}_i \vec{\sigma}_b] F^+) \otimes (F [\tilde{\rho}_i \vec{\sigma}_t] F^+ \vec{P}_t)) \end{aligned} \quad (19)$$

$$= 1/4 \sum_{i,j=0}^3 P_b^i P_t^j F [\tilde{\rho}_i (\sigma_b^i \otimes \sigma_t^j)] F^+, \quad (20)$$

where σ^0 denotes the unity 2×2 matrix and P_b^0 and P_t^0 are set to 1. To resolve the momentum part ($\tilde{\rho}_i$) of the density ρ_f one has to integrate over the initial momenta of the target and the spin particles, which leads to the initial momenta in F:

$$F = F(\vec{k}_i, \vec{k}_f) = \int F(\vec{k}, \vec{k}_f) \delta(\vec{k} - \vec{k}_i) d^3k. \quad (21)$$

Finally the differential cross section can be expressed as a function of the initial polarizations. With the initial momentum \vec{k}_i $d\sigma$ writes

$$d\sigma = Tr_{\Sigma} [F \rho_i F^+] \quad (22)$$

$$= 1/4 \left(\sum_{i,j=0}^3 P_b^i Tr_{\Sigma} [F \sigma_b^i \otimes \sigma_t^j F^+] P_t^j \right) \quad (23)$$

$$\begin{aligned} &= 1/4 (Tr_{\Sigma} [F F^+] + \vec{P}_b Tr_{\Sigma} [F \vec{\sigma}_b F^+] + \vec{P}_t Tr_{\Sigma} [F \vec{\sigma}_t F^+] \\ &+ \vec{P}_b Tr_{\Sigma} [F \vec{\sigma}_b \otimes \vec{\sigma}_t F^+] \vec{P}_t). \end{aligned} \quad (24)$$

2.3 Definition of A_{zx}

The splitting in equation 24 has important consequences for cross section measurements with polarized particles. The parts have the following meaning: The first term is the cross section for zero target and beam polarization, because the initial density for such an ensemble is just $\rho_i = 1/4 \hat{\rho}_i(1 \otimes 1)$. It will be written as $d\sigma_0$. The second term is independent of the target- and the third independent of the beam polarization. These parts of the cross section are

measurable, when the target or the beam (or both) are polarized. The last part is only measurable if one has both, polarized beam and polarized target. The terms have usually the following names:

$\vec{A}^b = \frac{1}{d\sigma_0} Tr_{\Sigma} [F \vec{\sigma}_b F^+]$ The **analyzing power** of the beam particles (neutrons).

$\vec{A}^t = \frac{1}{d\sigma_0} Tr_{\Sigma} [F \vec{\sigma}_t F^+]$ The **analyzing power** of the target particles (protons).

$\underline{A} = \frac{1}{d\sigma_0} Tr_{\Sigma} [F \vec{\sigma}_b \otimes \vec{\sigma}_t F^+]$ The **spin correlation matrix** of the beam and target particles (neutrons and protons).

\underline{A} is a 3x3 Matrix with the components:

$$[A]_{i,j} = \frac{1}{d\sigma_0} Tr_{\Sigma} [F \sigma_b^i \otimes \sigma_t^j F^+]. \quad (25)$$

$A_{zx} \equiv [A]_{z,x}$ is therefore the part of the interaction for which the spin of the neutron has the direction in \vec{e}_z - and for the proton in the target in \vec{e}_x normalized to the unpolarized cross section. In the Bystricky-notation A_{zx} would be A_{00ks} .

With these definitions the cross section has the well known form:

$$\boxed{d\sigma = d\sigma_0 (1 + \vec{P}_b \vec{A}^b + \vec{P}_t \vec{A}^t + \vec{P}_b \underline{A} \vec{P}_t)} \quad (26)$$

Assuming that the interaction conserves parity and is rotationally invariant, only a few components of the analyzing powers and the spin correlation matrix are non zero: namely A_t^y , A_b^y , A_{xx} , A_{yy} and A_{xz} , A_{zx} . If in addition the interaction is iso-spin invariant: $A_t^y = A_b^y$ and $A_{xz} = A_{zx}$.

To determine A_{zx} the asymmetry of the cross section is needed with the neutrons polarized parallel ($d\sigma^{\uparrow}$) and antiparallel ($d\sigma^{\downarrow}$) to \vec{e}_z , while the target is polarized parallel to \vec{e}_x .

All the parameters mentioned play a more or less important role for the correction of the measured asymmetry: Because the target magnetic field axis is turned by 12° away from the x-axis, the polarization of the target has a component in z-direction and therefore the cross section has a term with A_{zz} . The beam has additional polarization components in x and y, due to the precession of the neutron spin in the Faraday Cup magnetic field (see chapter 4.3) and in the polarized proton target field. (x',y',z) are coordinates in the fixed coordinate frame, which is defined by the beam axis and the target polarization. ϕ is

the angle between this plane and the scattering plane in the coordinate frame shown in figure 3. The z-axis is the same for both systems.

Because of the vertical size of the neutron detector, the effective target and beam polarizations are subject to small mean reductions. Since the center of the neutron detector is slightly higher than the beam, the angular average of terms with $\sin(\phi)$ do not fully vanish. The polarization in x' and y' of the beam and the target need to be projected and averaged over the acceptance of the neutron detector for the 5 measured angles. The target (\vec{P}_t) and beam polarization (\vec{P}_b) have the following components $\vartheta = 12^\circ$:

$$\vec{P}_b = \begin{pmatrix} \cos(\phi) & \sin(\phi) \\ -\sin(\phi) & \cos(\phi) \end{pmatrix} \begin{pmatrix} P_b^{x'} \\ P_b^{y'} \end{pmatrix} \quad (27)$$

$$\vec{P}_t = \begin{pmatrix} \cos(\phi) & \sin(\phi) \\ -\sin(\phi) & \cos(\phi) \end{pmatrix} \begin{pmatrix} P_t \cos(\vartheta) \\ 0 \end{pmatrix}. \quad (28)$$

The target has only polarizations in x and z direction in the fixed frame.

The angular average ($\langle f \rangle_\theta$) of a function f, that depends on ϕ or the scattering angle θ (e.g. $f(\phi) = \sin(\phi)$) is:

$$\langle f \rangle_\theta = \frac{\int_{V(\theta)} f(\phi(\vec{x}_d)) d^3 x_d}{\int_{V(\theta)} d^3 x_d}. \quad (29)$$

(\vec{x}_d) is a coordinate vector on the neutron detector and $V(\theta)$ the volume of the neutron detector acceptance at the measured mean angle θ .

With these definitions the cross sections ($d\sigma^\uparrow$) and ($d\sigma^\perp$) can be written as

$$d\sigma^\uparrow = d\sigma_0 (1 + (a_1 + a_2) A_y + a_3 A_{xx} + a_4 A_{yy} + a_5 A_{zz} + (a_6 + a_7) A_{zx}) \quad (30)$$

$$d\sigma^\perp = d\sigma_0 (1 + (a_1 - a_2) A_y - a_3 A_{xx} - a_4 A_{yy} - a_5 A_{zz} - (a_6 + a_7) A_{zx}), \quad (31)$$

with the factors:

$$a_1 = \mp \cos(\vartheta) \langle \sin(\phi) \rangle_\theta |P_t| \quad (32)$$

$$a_2 = \langle \sin(\phi) \rangle_\theta |P_b^x| \mp \langle \cos(\phi) \rangle_\theta |P_b^y| \quad (33)$$

$$a_3 = \pm \cos(\vartheta) |P_t| (-\langle \cos^2(\phi) \rangle_\theta |P_b^x| \mp \langle \cos(\phi) \sin(\phi) \rangle_\theta |P_b^y|) \quad (34)$$

$$a_4 = \cos(\vartheta) \langle \sin(\phi) \cos(\phi) \rangle_\theta |P_b^y P_t| \quad (35)$$

$$a_5 = \mp \sin(\vartheta) |P_b^z P_t| \quad (36)$$

$$a_6 = \pm \cos(\vartheta) \langle \cos(\phi) \rangle_\theta |P_b^z P_t| \quad (37)$$

$$a_7 = \sin(\vartheta) |P_t| (\pm \langle \cos(\phi) \rangle_\theta |P_b^x| + \langle \sin(\phi) \rangle_\theta |P_b^y|). \quad (38)$$

$P_t \cos(\vartheta)$ is the target polarization in x-direction and $P_t \sin(\vartheta)$ the target polarization in z-direction. The upper signs are for positive target-, the lower for negative target polarization.

Finally A_{zx} can be calculated by building the cross section asymmetry from equations 30 and 31

$$A_{zx} = \frac{1}{a_6 + a_7} (\epsilon_{\pm} - a_2 A_y - a_3 A_{xx} - a_4 A_{yy} - a_5 A_{zz}) \quad (39)$$

$$\epsilon_{\pm} = \frac{d\sigma^{\uparrow} - d\sigma^{\downarrow}}{2 d\sigma_0}. \quad (40)$$

By building the sum of equations 30 and 31 the unpolarized cross section $d\sigma_0$ can be extracted:

$$d\sigma_0 = 1/2 \frac{d\sigma^{\uparrow} + d\sigma^{\downarrow}}{1 \mp a_1 A_y}. \quad (41)$$

The careful discussion of the orientation of the polarizations and their signs is of importance, because it is not obvious from theory if A_{zx} is positive or negative in the angular region of the experiment. Therefore it is necessary to know the absolute polarization orientations to calculate A_{zx} with the correct sign. In equation 30 to 38, the signs are already correctly anticipated. A detailed study of the signs is done in sections 4.3 ff.

So far it was assumed, that all the incident neutrons have the same momentum. In the most general case, the beam- as well as the target-particles are distributed in momentum. In this experiment the neutrons have a distribution of their initial momentum k_i , which depends on the applied cut (see chapter 4.4), while the target is at rest in the lab frame. It will be shown that not only the interaction is momentum dependent but also the incident beam polarization. The mean of the beam polarization has to be calculated from the incident energy distribution $n(k_i)$. The cross section asymmetry ϵ_{pm} is assumed to be nearly constant within the applied cuts. with the normalized distribution $\int n(k_i) dk_i = 1$, the beam polarization the beam polarization is:

$$\vec{P}_b = \int_{lowcut}^{highcut} n(k_i) \vec{P}'_b(k_i) dk_i, \quad (42)$$

where $\vec{P}'_b(k_i)$ is the unweighted beam polarization.

2.4 Phase Shifts and Mixing Parameters

In general, the states of the two-nucleon-system are expanded in the basis of given angular momenta (l) and spin (s) or total spin (J). For comparison with

theoretical predictions or with other data through a phase shift analysis, A_{zx} has to be decomposed into phase shifts and mixing parameters.

Often the S-matrix is used for description of scattering [8, 9]. S is defined in terms of T or F (see equation 7):

$$S = 1 + 2i T = 1 + \frac{2i}{c(\vec{k})} F. \quad (43)$$

From this definition A_{zx} can be written as a function of S instead of F (see equation 25). The phase shifts are usually represented as a function of angular momentum l , the spin s , the total spin J and its z-component m_J . The conversion of S to this representation is explained in [19, 20, 21]. It allows to write the **S** matrix for example in the Blatt-Biedenharn form [22]:

$$S = e^{i\delta} e^{2i\epsilon} e^{i\bar{\delta}}, \quad (44)$$

where $\bar{\delta}$ is a diagonal matrix with the matrix elements of the phases δ_l and $\underline{\epsilon}$ a symmetric matrix with zeros on the diagonal and the mixing parameters ϵ_J . For a transition from states with fixed J , the S matrix has the form:

$$\begin{aligned} S_J &= \begin{pmatrix} e^{i\delta_{j-1,j}} & 0 \\ 0 & e^{i\delta_{j+1,j}} \end{pmatrix} \begin{pmatrix} \cos(2\epsilon_J) & i \sin(2\epsilon_J) \\ i \sin(2\epsilon_J) & \cos(2\epsilon_J) \end{pmatrix} \\ &\times \begin{pmatrix} e^{i\delta_{j-1,j}} & 0 \\ 0 & e^{i\delta_{j+1,j}} \end{pmatrix}. \end{aligned} \quad (45)$$

From this relation A_{zx} can be directly written as a function of the phase shifts δ_l and the mixing parameters ϵ_J . The knowledge about the phases and the ϵ_J from theoretical predictions allows us to compare them directly to A_{zx} . On the other hand, this formalism can be used to take A_{zx} into a PSA data base to fit the phases and mixing parameters together with other data available.

3 Experimental Setup

The measurement is performed at the low energy area C (NEC) at the Paul Scherrer Institute (PSI) in Villigen, Switzerland. Transversally polarized protons ($+\vec{e}_y$ or $-\vec{e}_y$) are produced in an atomic beam ion source [23] and injected into the Phillips Cyclotron. The sign of the polarization of the beam is changed every second to eliminate temporal variations of the beam polarization. The Cyclotron is working with a radio frequency (rf) of 50.6 MHz to produce a beam of 71 MeV protons. The beam is transferred into the experimental area NEC.

The layout of the experimental setup in the hall is shown in figure 4.

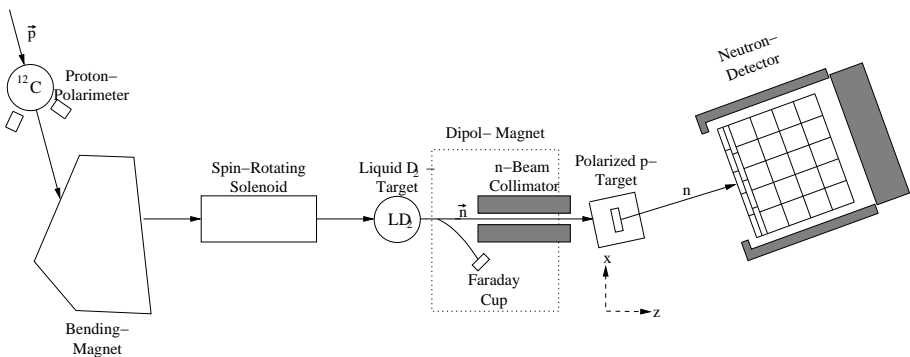


Figure 4: *Experimental setup of the experiment*

The beam enters the polarimeter chamber, where a $200\ \mu\text{m}$ carbon foil scatters protons to two Na-I detectors placed symmetrically left and right at 44° with respect to the beam direction. Due to the polarization flip, the polarization can be obtained from the cross section asymmetry of the detectors. This setup allows to measure polarization continuously with high precision (see reference [24] and section 4.1). A plastic scintillation detector is placed at 30° below the beam axis to monitor the time structure of the beam. The proton beam is then deflected by a dipole magnet and enters a solenoid, where its spin is rotated by 90° from the vertical into the horizontal direction. The experiment is performed with the magnetic field direction of the solenoid parallel and antiparallel to the beam to be insensitive to systematic effects.

After the spin rotation the beam enters the neutron production chamber, where it first passes a carbon collimator and a secondary electron emission monitor (SEM) [25]. The carbon collimator serves as a protection unit for the target. The SEM is a device for measuring the deviation of the beam position from the center. Its output currents can be used to directly adjust the steering magnets of the beam.

A liquid deuterium target (LD_2) is used to produce polarized neutrons via the $d(\vec{p}, \vec{n})pp$ - reaction (see section 4). The neutrons finally pass through a dipole magnet to turn their spins parallel (or antiparallel) to the beam axis. In addition the magnet deflects the remaining protons to a Faraday Cup (FC) to measure the beam current. The neutrons are taken through a brass collimator which leads to a beam spot of 19.2 mm diameter on the polarized proton target which is 3.6 m away from the LD_2 - target. The “neutron facility” at PSI is described in [26].

The scattered neutrons are measured by a segmented neutron detector 2.03 m away at an angle of 16.92° (see section 3.2). The recoil protons are measured in coincidence in the polarized target, which consists of a doped plastic scintillator serving as a polarized proton target and as a recoil detector (see section 3.1).

3.1 Scintillating Polarized Proton Target

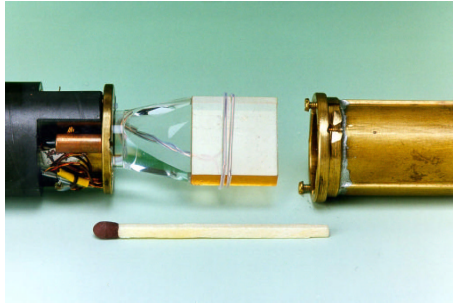
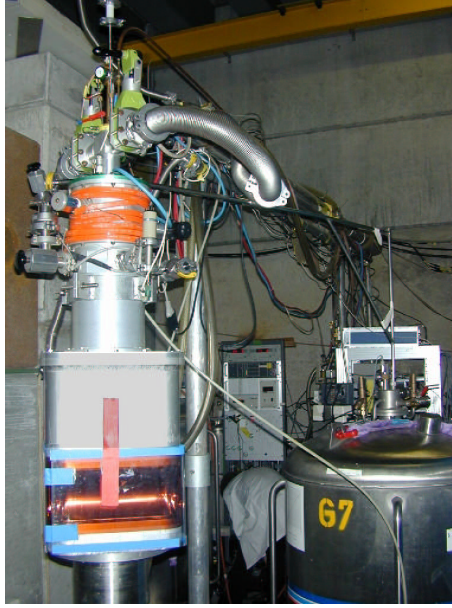


Figure 5: *Polarized proton target*

The polarized proton target is used as target and detector. This allows the measurement of the scattered neutrons in coincidence with the recoil protons. The background can significantly be reduced in comparison to previous single arm measurements [24].

The polarized proton target, built and operated by the polarized target group at PSI [27, 28], consists of a $5 \times 18 \times 18 \text{ mm}^3$ plastic organic scintillator doped with TEMPO, a free nitroxyl radical. The target is embedded into a He-cryostat to cool it down to 100 mK (figure 6). Coils of a superconducting magnet are defining the polarization direction of the target. With a concentration of 2×10^{19} paramagnetic centers per gram and a magnetic field of 2.5 T at a temperature of 100 mK, the target reaches a polarization up to 69% in the present experiment. The polarization is measured every 10 minutes by nuclear magnetic resonance (NMR) directly at the target. The polarization measurement via NMR has a systematic uncertainty of 2%, which is not significant

Figure 6: *Polarized target cryostat*

for the final results. The mean polarizations measured in the two parts of the experiment are shown in table 1.

The recoil protons have to be detected down to 2 MeV. It is necessary to

	Polarization [%]	Error
A_{zx} 99	57.04	2.00
A_{zx} 00	68.00	2.00

Table 1: *Mean target polarization of the two experimental runs A_{zx} 99 and A_{zx} 00*

obtain a sufficient light output to the detector, because the TEMPO reduces the light output of the target to a fifth of an undoped sample. The doped scintillator is glued to a fishtail shaped light collector. A 1 m long and 12 mm diameter plexiglass tube transports the light to a photomultiplier at the top of the cryostat (see figure 5). The diameter of the light-guide was limited by the design of the cryostat. In the two parts of the experiment the polarization was chosen once parallel to \vec{e}_x and once antiparallel to avoid systematic effects.

Geometric restrictions made it necessary to turn the cryostat by 12° to the neutron detector in order to have the scattered neutrons not hit one of the coils

of the magnet. Thus the target polarization has not only a component in x direction but also in z .

3.2 Neutron Detector



Figure 7: *The left picture shows the neutron detector from the front. On the right side the neutron detector in the lead house is shown from the front*

The neutron detector consists of an array of 20 scintillator bars of size $10 \times 10 \times 50 \text{ cm}^3$. They are vertically arranged with a width of 5 and depth of 4 bars (5 columns and 4 rows) as can be seen in Figure 7. On each side of the bars a light-guide collects the scintillation light to transport it to a photomultiplier (PM). The two-sided readout allows for a vertical position measurement, because the difference in time between the bottom and the top PM in a bar depends on its position. This was used in experiments at the Mainz Microtron in Mainz (MAMI) (see reference [29]). For the present experiment a position measurement is not necessary.

In front of the bars there are two layers of totally 9 thin (1 cm thick) scintillation detectors (ΔE -detectors) for discriminating protons from neutrons.

The detector is shielded from the hall background by 2×5 cm thick lead plates (except for a 50×50 cm² window at the front). On the backside the shielding is performed by a massive concrete block. The front of the bars is 203.3 cm away from the pivot, where the ΔE 's have a distance of 193.3 cm. The center of the detector is 5.5 cm higher than the beam, which leads to slightly different scattering angles than in the symmetrical case.

The arrangement allows a measurement at 5 different angles: from 9.91° (minimal lab angle) to 25.2° (maximal lab angle), with a mean solid angle of 10 msr. The mean lab angles for the bars are: 12.41° , 15.03° , 17.56° , 20.10° and 22.41° .

The neutrons in the bars undergo a scattering or a reaction with hydrogen or carbon in the scintillator before being detected. See [30] for a detailed description of the processes involved. A measurement of the energy of the individual neutrons via the light output of the scintillators is therefore not possible. The energies detected in the bars range up to the maximal energy, that can be deposited in the bars. In figure 8 such a spectrum is shown for one bar. The measurement of the time of flight (TOF) is the only possibility to distinguish between different neutron energies.

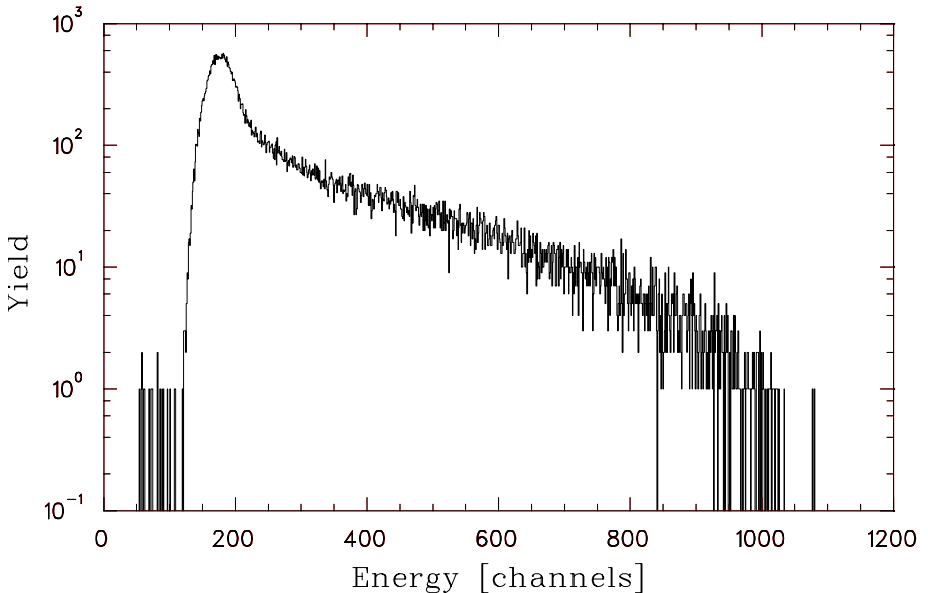


Figure 8: *Typical ADC neutron spectrum from a PM of the neutron detector*

4 Analysis

The analysis section covers the determination of the proton beam polarization, which is necessary to calculate the polarization of the neutrons. The determination of the absolute direction of the final neutron polarizations for the two spin directions (0) and (1) is shown. The main analysis is discussed in two parts: first the neutron energy distribution, which is essential for the knowledge of the proton- neutron spin transfer and the spin rotation in the Faraday Cup (FC) magnetic field. The second part explains the main cuts applied to the target time and the time of flight from the target to the neutron detector. Further, dead time and beam current corrections are discussed as well as false asymmetries arising from them. An asymmetry investigation of the background is done and finally a short discussion of the scattering of neutrons off ^{12}C is given.

Note that all values presented in % are absolute as long as not otherwise mentioned.

4.1 Beam Polarimeter

The beam polarization is measured by determining the polarization asymmetry of the cross section from the $^{12}\text{C}(\vec{p}, p)$ -reaction for two different polarization states. As mentioned in section 3 the protons are detected in Na-I scintillation detectors left and right of the beam axis at an angle of 44° where the analyzing power of the reaction [31] is maximal. The outputs of the Na-I detectors are fed into analog to digital converters (ADC) after amplification. The signals of the ADC's, which are proportional to the input energies of the protons, are then collected in Borer Buffers. In addition a pulser signal is added to the input. By recording this pulser in a scaler at the same time, the yields can be dead time corrected. This is done for each polarization state independently (see figure 9). Figure 10 shows the energy spectrum of the left Na-I detector for the two spin states. The elastically scattered protons are detected with the highest energy and show a strong asymmetry due to the spin-orbit coupling, while scattering from the first excited state (4.4 MeV lower) is independent of the spin.

There is a slight shift visible in the pulse height of the two spin states, which is an indication that there is a small left-right asymmetry of the beam position. For the polarization measurement this effect is not of any importance (except for the adjustment of cuts), but it has some relevance for false asymmetries explained in chapter 4.7.

For obtaining cross sections, the counts in the elastic peak are, for each spin state separately, normalized to the signal of the Faraday Cup (FC) which is proportional to the integrated beam current.

The polarization of the protons can be calculated as follows: If $\sigma(0)$ denotes the cross section with spin in $+\vec{y}$ - and $\sigma(1)$ in $-\vec{y}$ -direction, the cross sections

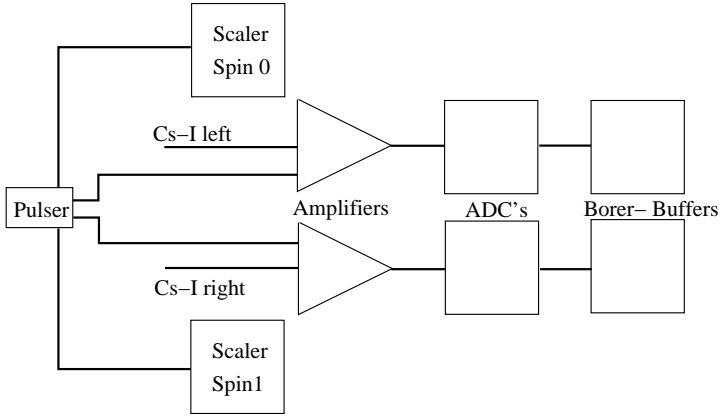


Figure 9: *The trigger electronic setup from the proton polarimeter.*

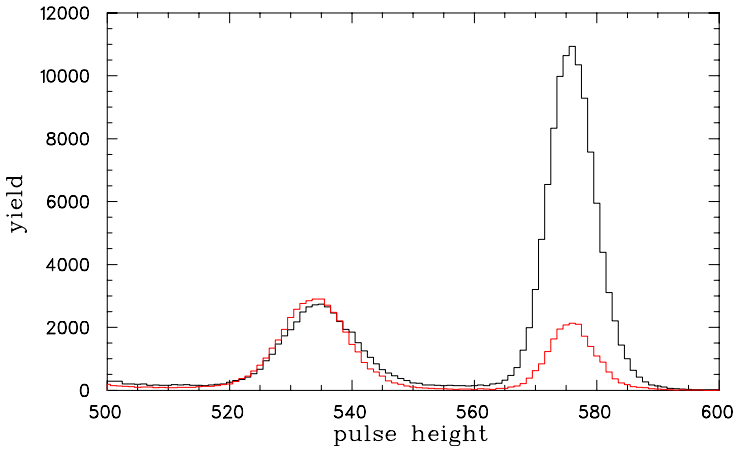


Figure 10: *Energy spectrum of the left Na-I for the two spin states in the proton polarimeter. Black: spin state 0; Red: spin state 1*

can be written as (see section 2.2):

$$\sigma^i(0) = \sigma_0^i (1 + A_y^i P(0)) \quad (46)$$

$$\sigma^i(1) = \sigma_0^i (1 + A_y^i P(1)) \quad (47)$$

$$\implies \sigma_0^i = 1/2 (\sigma^i(0) + \sigma^i(1)). \quad (48)$$

σ_0^i denotes the unpolarized cross section, and i the number of the detector.

The calculation of the polarization can be done for each detector separately or by using the super-ratio method. The former method is straight forward: Assuming that the polarizations of state 0 and 1 are the same (with opposite sign $P(0) = -P(1)$), P can be calculated from equations 47 and 48 to:

$$P = \frac{1}{2 A_y^i} \frac{\sigma^i(0) - \sigma^i(1)}{\sigma_0^i}. \quad (49)$$

The super-ratio method takes the polarization measurement of both detectors into account. From parity invariance of the scattering process the analyzing powers for the right and the left detector have equal strength: $A_y(+44^\circ) = -A_y(-44^\circ)$. From the ratios of the cross sections the polarization can be extracted:

$$\frac{\sigma^l(0)}{\sigma^l(1)} \cdot \frac{\sigma^r(1)}{\sigma^r(0)} = \frac{1 + A_y P(0)}{1 + A_y P(1)} \cdot \frac{1 - A_y P(1)}{1 - A_y P(0)}. \quad (50)$$

Thus the norm of the polarization is given by:

$$|P| = \frac{1}{A_y} \frac{w - 1}{w + 1} \quad (51)$$

$$\text{with } w = \sqrt{\frac{\sigma^l(0) \sigma^r(1)}{\sigma^l(1) \sigma^r(0)}}. \quad (52)$$

The super-ratio method allows to determine the polarization with smaller statistical error than the normal method, but it is not sensitive to a difference in polarization of state 0 and 1. The first calculation indicates whenever $P(0) \neq P(1)$ from a difference in the left-right asymmetry:

$$P^l = \frac{1}{A_y} \frac{\sigma^l(0) - \sigma^l(1)}{\sigma^l(1) + \sigma^l(0)} = \frac{P(0) - P(1)}{2 + A_y(P(1) + P(0))} \quad (53)$$

$$P^r = \frac{1}{A_y} \frac{\sigma^r(1) - \sigma^r(0)}{\sigma^r(1) + \sigma^r(0)} = \frac{P(0) - P(1)}{2 - A_y(P(0) + P(1))} \quad (54)$$

The difference in the polarization states can be directly calculated from the ratio P^l/P^r :

$$\Delta P := |P(0)| - |P(1)| = 2 \frac{1 - P^l/P^r}{1 + P^l/P^r}. \quad (55)$$

The mean relative difference ($\Delta P/P$) in the experiment is in the order of 0.5%. This relatively small asymmetry allows to use the mean polarization obtained via the super ratio method. This difference is not important for A_{zx} , because the asymmetry is small and goes with $1/P$ (see equation 39).

Although the measurement is nearly free of background the polarization is calculated in three different ways in order to be independent of the method:

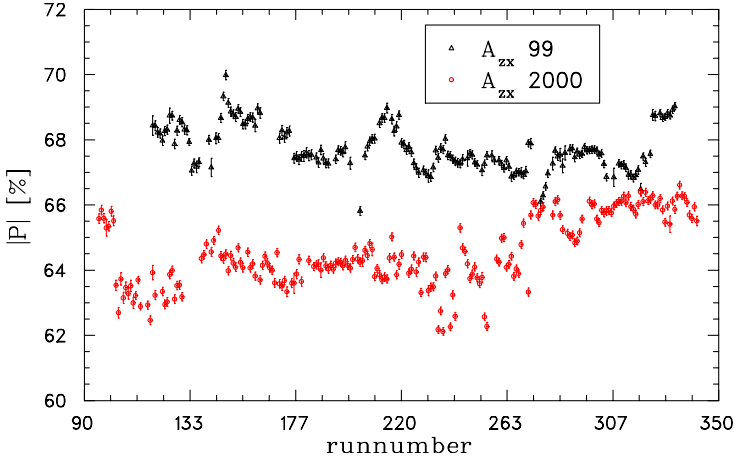


Figure 11: Polarization as a function of the run numbers from the two experimental periods A_{zx} 99 and A_{zx} 00.

	Super-ratio	ΔP_{stat}	ΔP_{sys}
A_{zx} 99	67.717 %	0.0099 %	0.186 %
A_{zx} 00	64.606 %	0.0088 %	0.166 %

Table 2: Beam polarization of the Experiment from the two run periods November '99 and March '00

The first calculation is made without any background subtraction, the second is done with a straight line background subtraction (no fit) and the third is achieved with fitting a Gaussian with linear background. The polarization is slightly reduced by the background, as expected, by 0.4%. The difference between the fit and the straight line subtraction is smaller than 0.2%. Figure 11 shows the polarizations calculated with the super-ratio method for the two different run periods. In table 2 the mean polarizations from the super-ratio method are taken for the calculation of A_{zx} with the statistical error ΔP_{stat} and the systematical error ΔP_{sys} resulting from the difference in the polarization states discussed above.

4.2 Electronic Setup

The signals, coming either from the neutron detector or from the target, carry information about the energy and the time at which the particle was detected. One part of the signals is fed into ADC's (Analog to Digital Converter) after

multiplexing with linear Fan's and appropriate delay, the other part is converted into logical signals by discriminators to define the time (see figure 12). Because the signals are relatively small and noisy in the target detector a constant fraction discriminator (CFD) is used to make sure that the time is independent of the signal height. One output is used to stop the TDC's (Time to Digital Converter), another one to feed the scalers, which count each incoming signal.

The upper and lower PM of each bar of the neutron detector are taken in coincidence to reject low energy background and noise. All 20 bars are linked together with a logical OR. To assure that the target time is taken as the coincidence time, the neutron detector time width is 42 ns, where the target signal is only 2 ns broad. This opens the possibility to measure coincidences with different beam bunches, which are 20 ns apart from each other. These coincidences are only accidental and can therefore be used for background measurement. An additional coincidence with the cyclotron RF signal is taken to reduce accidentals which are not correlated with the beam bunch. This signal defines the so called "pre-trigger" which is fed into a scaler. The RF signal itself is taken in coincidence with the signal from the Faraday Cup to make sure that only triggers are generated, when the beam is on. To define a time zero a further coincidence with the RF is performed, to make sure that the leading edge of the RF-signal is really the start for the TDC's. This coincidence is vetoed by the "computer busy" and is the "trigger" signal for all Camac modules. It is possible to measure the dead time of the data acquisition by comparing the counts from the scalers of the pre-trigger and the trigger. With an additional coincidence with a signal which is set, when a run is started, the frontend computer is forced to read out the modules. The veto detectors (ΔE) are only read out and have no share in the trigger.

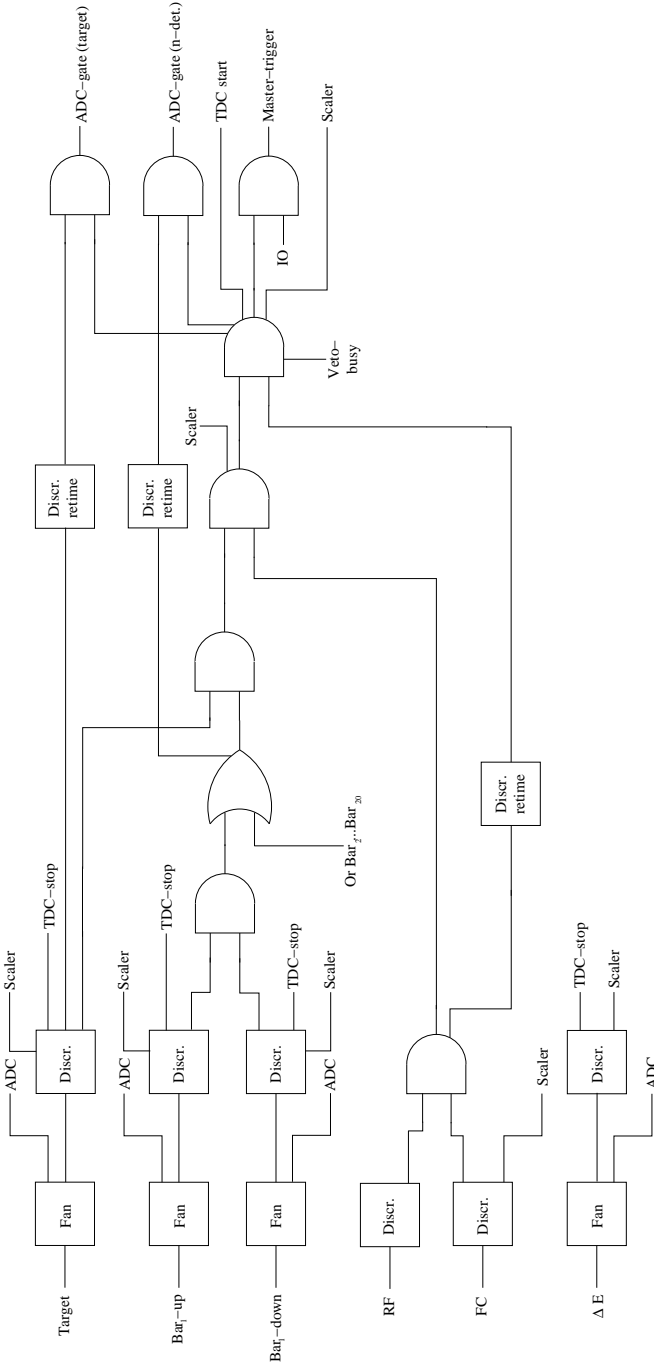


Figure 12: Trigger electronics of the experiment

4.3 Determination Of The Sign Of The Neutron Beam Polarization

Since the A_{zx} is small, it is not clear from existing phase shift analyzes, if its value is positive or negative. Only the knowledge of the polarization direction for the two spin orientations can determine the correct sign.

From elastic $^{12}C(\vec{p}, p)$ scattering in the polarimeter, the spin orientation of the proton can be determined. The proton is polarized perpendicular to the scattering plane either to the ceiling or the floor. In terms of the coordinate frame introduced in figure 3, the scattering to the left detector shall be considered (looking in direction of the incident proton momentum). Thus the y-axis ($\vec{e}_y = \vec{k}_i \times \vec{k}_f$) is pointing to the ceiling. Since the neutron detector is on the left side as well, that frame provides a good choice. Scattering to the right detector is described by a negative scattering angle θ .

Because the spin-orbit force is attractive in $^{12}C(\vec{p}, p)$, A_y is positive for the left Na-I detector. The spin orientation in $+\vec{e}_y$ is thus the one with bigger cross section (see equation 47).

A different explanation can be given looking directly at the spin orbit Hamiltonian. With \vec{L} and \vec{S} the angular momentum and the Spin- operators H_{s-o} is:

$$H_{s-o} \propto -\vec{L} \cdot \vec{S}. \quad (56)$$

For the left Na-I $\vec{L} = \vec{r} \times \vec{k}_i$ points to +y (ceiling), because the protons going to the left would pass the ^{12}C - nucleus from the right side (see this argumentation in [32]). With the spin orientation parallel to $+\vec{e}_y$ (and therefore parallel to \vec{L}), H_{s-o} would be negative. In this case the elastic cross section would be larger than for the antiparallel situation. This implies that the spin in y direction is the one with bigger cross section in the left detector (see figure 10). The same argument holds for the right detector, but there with opposite sign. The proton ensemble with orientation in $+\vec{e}_y$ direction will be called spin state 0 (ρ_y^p) and in $-\vec{e}_y$ direction 1 (ρ_{-y}^p) in the experiment (see chapter 4.1).

The spin of a particle with magnetic moment \vec{m} will be turned in a magnetic field due to the torque (\vec{M}) acting on the magnetic moment (see also the calculation in Appendix A):

$$\vec{M} = \langle \vec{m}_i \rangle_{\rho_i} \times \vec{B} = \frac{d \langle \vec{S} \rangle_{\rho_i}}{dt} \quad (57)$$

$$\vec{m}_i := g_i \mu_k \vec{S}, \quad i \in \{p, n\} \quad (58)$$

\vec{m} can be proportional or anti proportional to the spin depending on its g-factor (g_i), which is positive for the proton and negative for the neutron.

After the proton beam has left the polarimeter it is turned by 90° passing a solenoid (see figure 4). Its magnetic field direction points either in \vec{e}_z or $-\vec{e}_z$.

It has been switched several times during the experiment to avoid systematic effects.

Thus the resulting orientations for the two settings of the solenoid field and the spin orientations in the proton ensembles ρ_y^p and ρ_{-y}^p are presented in table 3. In the neutron production target the proton polarization is transferred to the

		Proton pol.	
		$+\vec{e}_y$	$-\vec{e}_y$
Sol.-	$+\vec{e}_z$	$+\vec{e}_x$	$-\vec{e}_x$
field	$-\vec{e}_z$	$-\vec{e}_x$	$+\vec{e}_x$

Table 3: Orientation of the proton spins after passing the Solenoid field

neutrons in **opposite** direction (see section 4.4 for details). The polarization is turned further in the Faraday Cup magnetic field, which is pointing to $+\vec{e}_y$. Because the neutron has a negative g-factor, the magnetic moment \vec{m} is in opposite direction of its polarization. From equation 58 the torque is in $-\vec{e}_z$ direction for initially in $+\vec{e}_x$ polarized neutrons and vice versa.

Taking the information from table 3, the negative spin transfer of the proton to the neutron and the neutron spin rotation together, the resulting neutron polarization from initially polarized protons is presented in table 4

		Proton pol.	
		$+\vec{e}_y$	$-\vec{e}_y$
Sol.-	$+\vec{e}_z$	$+\vec{e}_z$	$-\vec{e}_z$
field	$-\vec{e}_z$	$-\vec{e}_z$	$+\vec{e}_z$

Table 4: Spin direction of the neutrons after the FC-field as a function of the initial proton polarization and the solenoid field direction

The magnetic field of the target has a large influence on the final polarization orientation of the neutrons, because it is nearly oriented perpendicular to the z - y plane. The B-field is $\vec{B}_t = |B_t|(\pm \cos(\vartheta), \mp \sin(\vartheta))$ in the x - z plane, with $\vartheta = 12^\circ$. The upper signs are for positive, the lower for negative target polarization. The Helmholtz-shaped field distribution has nearly a constant B-field over a range of 10 cm, with a strength of $|B_t| = 2.49T$, which results in a significant contribution of a y -component of the neutron polarization at the target, see section 4.5.

4.4 The Neutron Energy Distribution

The neutrons produced in the reaction $D(\vec{p}, \vec{n})pp$ at zero degrees have a momentum distribution with a low energy tail due to the three body breakup reaction of the d+p system, even if the initial protons are nearly monoenergetic. The momentum distribution is known [26] and can be adapted by a Monte Carlo (MC) simulation to the given experimental conditions. The momentum dependent spin transfer from the initial protons to the neutrons $K_x^{x'}$ ($\equiv K_{0s''s_0}$ in the Bystricky notation) at 0° has been measured to an accuracy of 1.1% [33]. Figure 13 shows both, the energy distribution of the reaction $D(\vec{p}, \vec{n})pp$ and $K_x^{x'}$.

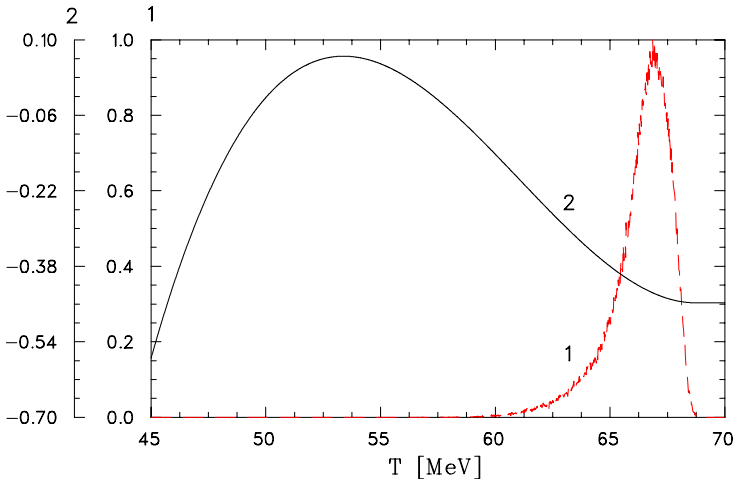


Figure 13: The n - p spin-transfer $K_x^{x'}$ (2) and the neutron distribution $n(T)$ (1) as a function of the neutron kinetic energy T .

The neutron flight time from the production target to the proton target is not directly measured; instead, the time between the cyclotron RF and the target is registered. The time resolution for the neutrons is broadened by experimental effects like the PM time resolution and the photon transit time from the detector to the PM. The resolution can be accounted for using a MC simulation in order to fit the measured timing resolution in the experiment (see figure 14). The simulation gives a total resolution of 1 ns “full width half max” (FWHM). Thus the MC allows to simulate the time or energy distribution of the neutrons for any cut in the experimental target time spectrum and with it allows to extract the corresponding spin transfer.

The resulting polarization of the neutrons is not only determined by the initial proton polarization and a correct $K_x^{x'}$ but also by the energy dependent

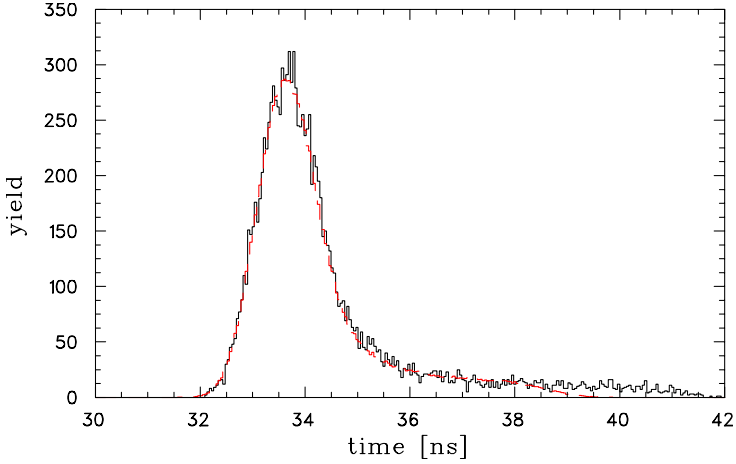


Figure 14: *Target time spectrum (black) and Monte Carlo simulated spectrum (red dashed line).*

spin rotation in the FC- and the target-magnetic field. In this chapter the focus is mainly on the spin rotation in the FC field.

From the knowledge of the field ($B_y = 0.476 \text{ T}$) and the length over which it is acting ($\Delta z = 1.95 \text{ m}$), the corrected polarization can be calculated. The polarization rotation of an initially in $+\vec{e}_x$ or $-\vec{e}_x$ polarized beam depends on the rotation angle $\Lambda := \frac{1}{2\hbar} g_n \mu_k B_y \Delta t$ with negative g-factor g_n for the neutron (see Appendix A):

$$\vec{P}_b = \pm |P_x| \begin{pmatrix} \cos^2 \Lambda - \sin^2 \Lambda \\ 0 \\ 2 \sin \Lambda \cos \Lambda \end{pmatrix} \quad (59)$$

The time Δt during which the neutrons are in the field can also be expressed as a function of the kinetic energy T . Relativistically it follows that:

$$\Delta t = \frac{\Delta z}{c} \sqrt{\frac{m_n^2 + T^2 + 2 T m_n}{T^2 + 2 T m_n}}, \quad (60)$$

where m_n is the neutron rest mass in MeV and c the speed of light in the vacuum. In figure 15 the neutron polarization in x and z direction of a 100% polarized neutron beam in $-\vec{e}_x$ is shown as a function of T . Note that the sign is the same for P_x and P_z for energies below $< 68 \text{ MeV}$. A cut of 3 ns around the peak in the target TDC in figure 14 corresponds to an energy distribution shown in figure 16. The beam is polarized to 100% in \vec{e}_z - direction at an energy of 67.9 MeV, where the peak maximum in the distribution function $n(T)$ (see

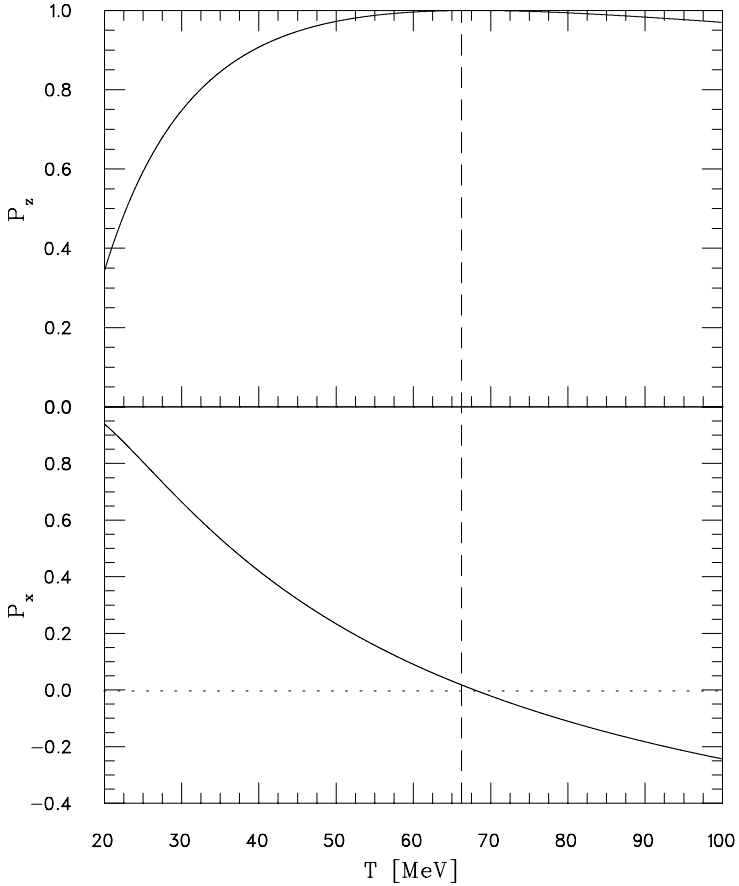


Figure 15: Neutron polarization in \vec{e}_z - (top) and in \vec{e}_x -direction (bottom) after the FC field from a 100% polarized beam as a function of the kinetic energy T after passing the Faraday Cup magnetic field. The dotted vertical line indicates the mean neutron energy.

figure 15) is 1 MeV lower. Nevertheless P_z is slowly decreasing to lower energies and therefore the weighted polarization is still near 100%.

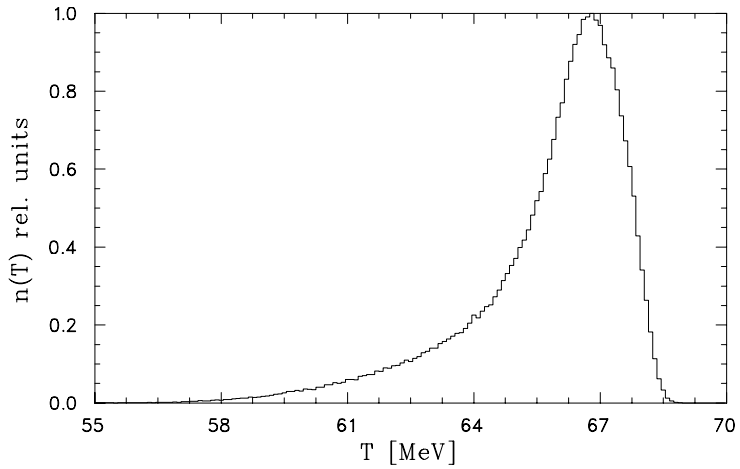


Figure 16: *MC-simulated energy distribution from a 3 ns target time cut.*

4.5 The Effect Of The Target-Magnetic Field

The magnetic field of the polarized proton target plays an important role for the final polarization direction of the neutron beam, because the field is nearly perpendicular oriented to the polarization. In figure 17 the map of the field is shown in the frame of the target. As explained in section 3.1, the target is turned by 12° in the x-z plane, so that the neutrons do not have a symmetry axis as flight path, but a path indicated by the blue line. The magnetic field

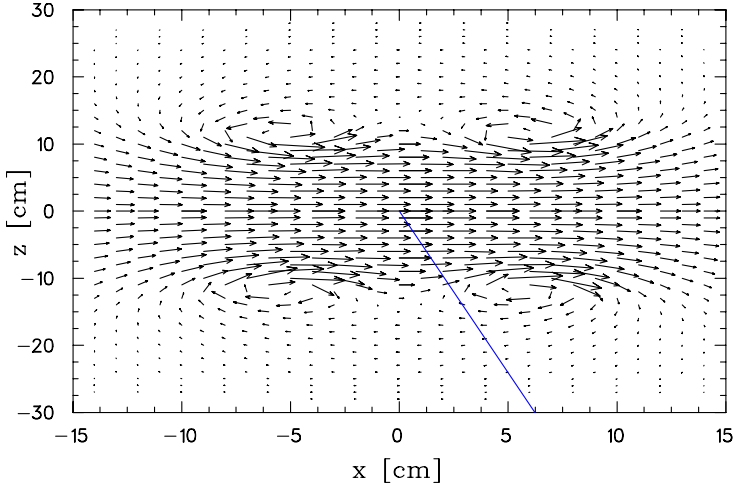


Figure 17: *Target magnetic field. The arrow lengths are proportional to the field strength. x and y are coordinates in the target frame. The blue line indicates the flight path of the neutrons.*

strength in x and z direction (B_x and B_z), which the neutrons see, flying towards the target, are shown in figure 18. For a positively ($+\vec{e}_z$) polarized neutron after the FC field, the spin is first turned towards $-\vec{e}_y$ until the beam reaches the inner part of the coils at 10 cm, where it is forced towards $+\vec{e}_y$ with a field of 2.4 T.

In order to calculate the neutron polarization, the Schrödinger's equation is integrated numerically, taking into account the target field at each point of the path. The calculation is done in the frame of the neutron, flying with energy T . The relation between position, time and energy is already explained in equation 60, so that the target field operator can be expressed time dependently:

$$\frac{d}{dt}|\psi(t)\rangle = -\frac{i}{\hbar}H|\psi(t)\rangle \quad (61)$$

$$H = -g_n\mu_k S_x B_x(t) + S_z B_z(t). \quad (62)$$

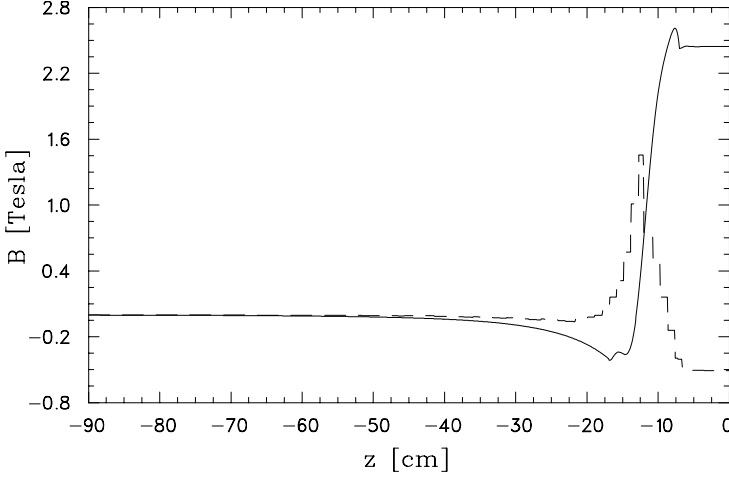


Figure 18: The field strengths B_x (solid line) and B_z (dashed line) of the target as seen from the neutrons along their flight path (along the blue line of figure 17).

As initial state ($|\psi\rangle_0$) for the numerical integration, the neutron polarization after the FC field is taken, which is given in equation 89 or 90. The integration procedure is explained in appendix B.

The polarization at the target is again depending on the incident energy after the D_2 -target. The energy dependence is shown in figure 19 for a 100% in $-\vec{e}_x$ polarized neutron beam before the FC-field, with the magnetic field of the target in $+\vec{e}_x$. The main effect of the target field is the polarization component p_y and a small reduction in p_z . The polarization in p_x is small at the measured mean energy, but depends strongest on the applied time cut of the target time.

The energy weighted ($n_b(T)$) polarization of the neutron beam, taking into account the energy dependent spin transfer $K_x^{x'}(0^\circ)$ in the deuterium target, the energy dependent rotation in the FC field B_y and the energy dependent rotation in the target field, is therefore obtained by folding all functions and multiplying with the proton polarization P :

$$\vec{P}_b = P \int_{lowcut}^{highcut} n_b(T) K_x^{x'}(0^\circ) \begin{pmatrix} \langle \psi(T) | \sigma_x | \psi(T) \rangle \\ \langle \psi(T) | \sigma_y | \psi(T) \rangle \\ \langle \psi(T) | \sigma_z | \psi(T) \rangle \end{pmatrix} dT \quad (63)$$

The energy dependent state $|\psi(T)\rangle$ is the spin state at the target.

Not only the polarization \vec{P}_b is depending on the cuts, but also A_{zx} . The upper cut (“highcut”) is varied around the typical 3 ns value for obtaining the

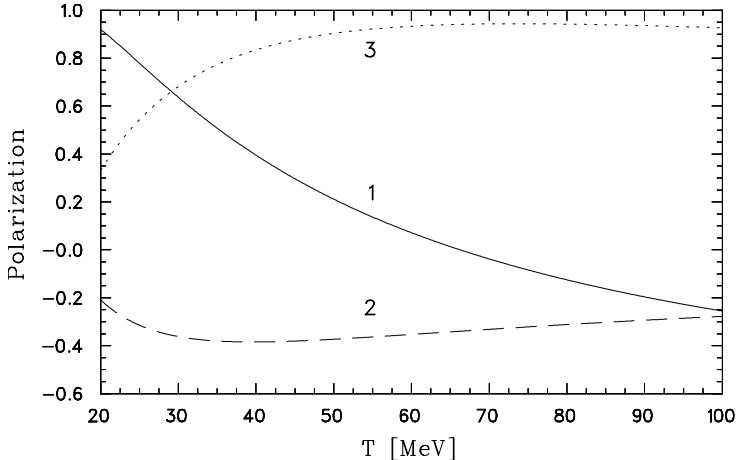


Figure 19: Polarization of a neutron beam, initially 100% polarized in $-\vec{e}_x$ after the D_2 -target as a function of the energy. (1) p_x , (2) p_y , (3) p_z . The target has positive polarization.

mean. Because A_{zx} is energy dependent itself, the uncertainty is given in the standard deviation of the distribution $n(T)$ from figure 16 (see Appendix C).

4.6 Main Cuts

Due to the fact that we measure the protons and neutrons in coincidence, the background is already reduced by a big amount. Cuts are mainly applied to the target time (t_t) (see last chapter) and to the time of flight of the neutron (TOF), where TOF is the difference of the neutron time (t_n) and t_t . In the Figures 20 and 21 the yield of the target time and the TOF is shown for one bar. The two-dimensional view shows all the timing characteristics of this experiment. The width of 42 ns in the coincidence window of the neutron detector opens the possibility to measure accidental coincidences from earlier beam bunches which are 20 ns apart from each other.

The lines with negative slope in figure 20 (1+2) arise from random coincidences, where the neutron time is constant but the target fires at random times, because of its low threshold in the CFD. The desired n-p coincidences are in the main peak of the histogram (3), while the low energy neutron tail can be seen in the line with positive slope (4). The fact that the target is mainly composed of plastic scintillator, not only n-p scattering occurs but also scattering and reactions of neutrons on ^{12}C . The main reaction $^{12}C(n, np)^{11}B$ is assumed to produce the main part of the coincident background (5). Fortunately the neutrons from this reaction are at least 3 ns slower than from the direct n-p

scattering and can therefore be separated. See chapter 4.8 for a discussion of this background. The desired n-p events can be directly chosen by cutting on

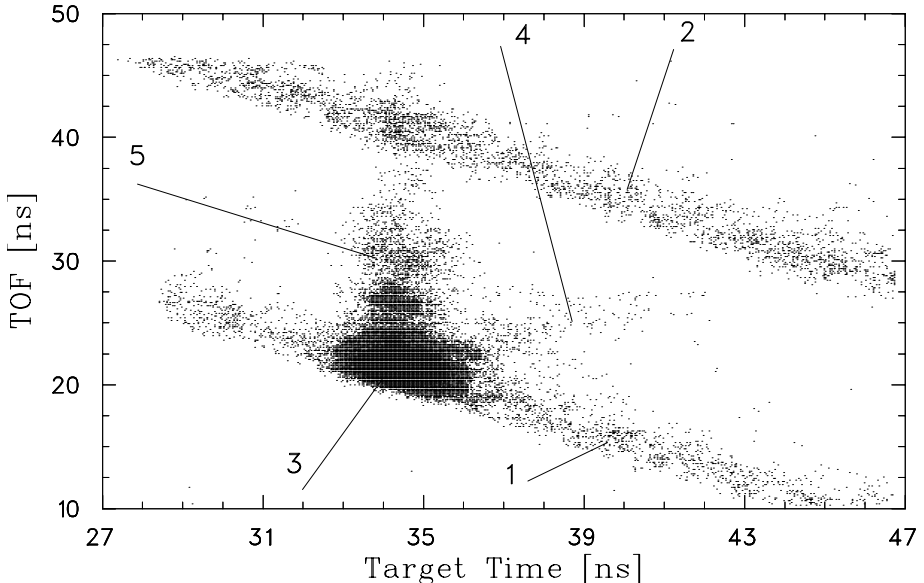


Figure 20: *Neutron TOF versus target time: (1) accidental coincidences from the same beam bunch, (2) accidental coincidences with an earlier beam bunch, (3) n-p coincidences, (4) n-p elastic line, (5) n-¹²C scattering.*

peak (3) for each polarization state and each column of 4 bars in the neutron detector. Typically a cut 3 ns wide in the target time and 3 ns in the TOF is used. These cuts can be applied to the target energy spectrum. Depending on the scattering angle (or the column), the recoil protons have different energies (see figure 22). The low energy background in the ADC spectra is mainly a consequence of the random coincidences discussed. A cleaner 2-dimensional time spectrum results (see figure 23) when cutting the low energy background away. The remaining background below the n-p peak can directly be subtracted using the random coincidences with an earlier beam bunch (2).

Charged particles which could also trigger the neutron detector are discriminated against neutrons by demanding, that the ΔE s in front of the bars do not fire.

To improve the time resolution in the TOF, very low energy events are cut in the neutron bar ADC's to ensure that amplitude walk effects [34] are minimized. A typical neutron ADC spectrum has been shown already in figure 8.

In 0.6% of the cases it happens that the bars from several columns fire and

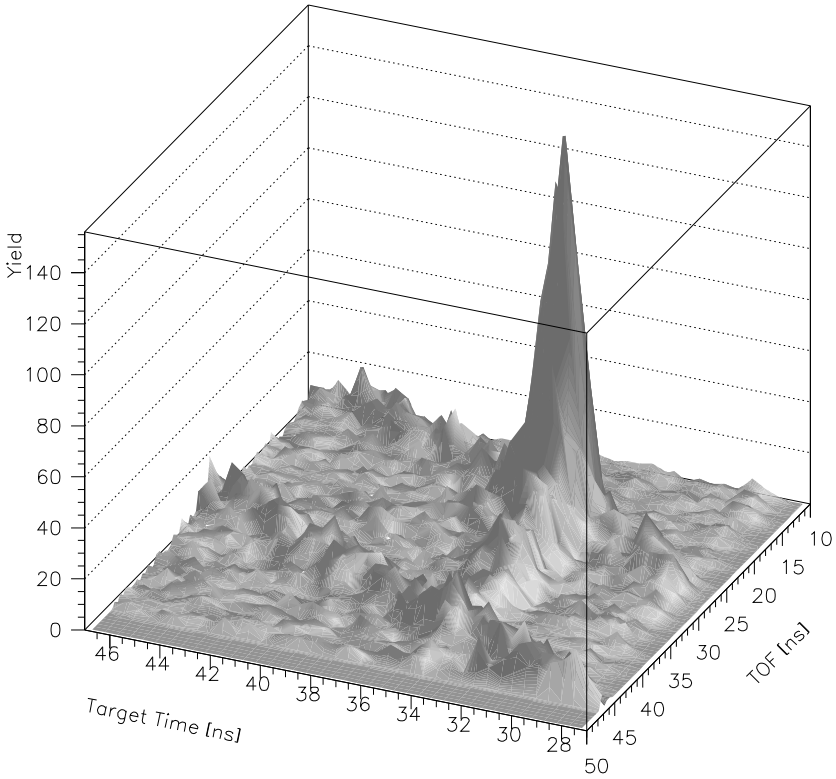


Figure 21: *TOF versus Target time (same histogram as figure 20).*

fulfill the conditions defined by the cuts. These events are excluded. But as long as the multiple hits occur in the same column, the events are taken and counted as a single event for this angle.

4.7 Normalization, Dead Time Correction and False Asymmetries

The yields resulting for the two polarizations after applying the cuts discussed in the last section have to be normalized to the individual currents for each polarization. In addition the trigger (t_r) and pre-trigger (p_{tr}) values (see section

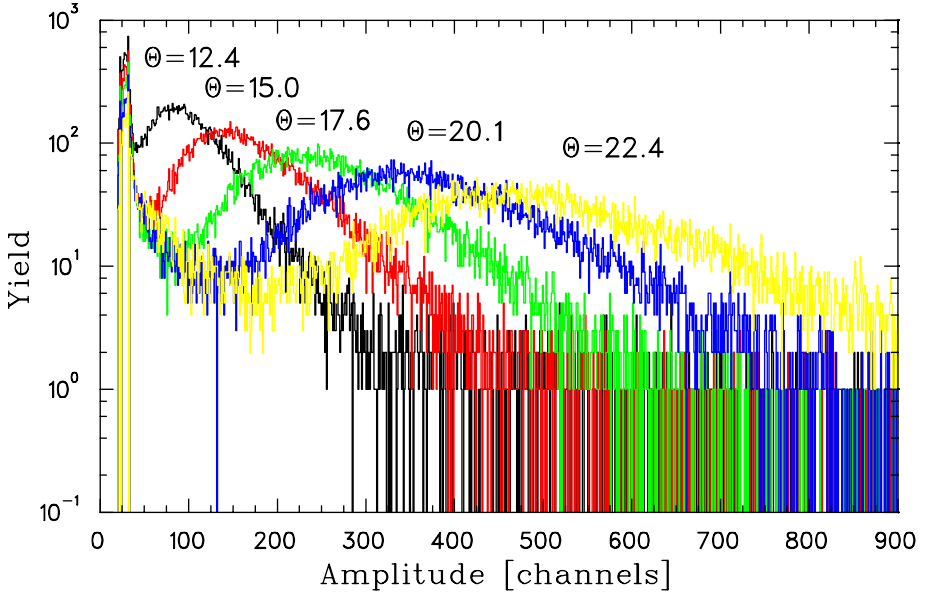


Figure 22: Target ADC spectra for the 5 neutron detector angles after cutting on the n - p elastic peak.

4.2) can be used to correct for computer dead times:

If N_i is the uncorrected yield for polarization $i = 0$ and 1, the corrected yields \tilde{N}_i are given by:

$$\tilde{N}_i = d(i) \frac{N_i}{FC(i)} \quad (64)$$

$$d(i) := \frac{p_{tr}(i)}{t_r(i)}. \quad (65)$$

Here FC are the charges integrated in the Faraday Cup. These values are used to calculate the asymmetry ϵ (see equation 39):

$$\epsilon = (1 \mp a_1 A_y) \frac{\tilde{N}_1 - \tilde{N}_0}{\tilde{N}_1 + \tilde{N}_0} \quad (66)$$

Because of the small expected value for A_{zx} it is important to check and correct the experiment for false asymmetries arising from minimal deviations in the beam for the two polarizations or from big dead-time corrections. For the investigation of this problem the asymmetries of the corrections themselves are

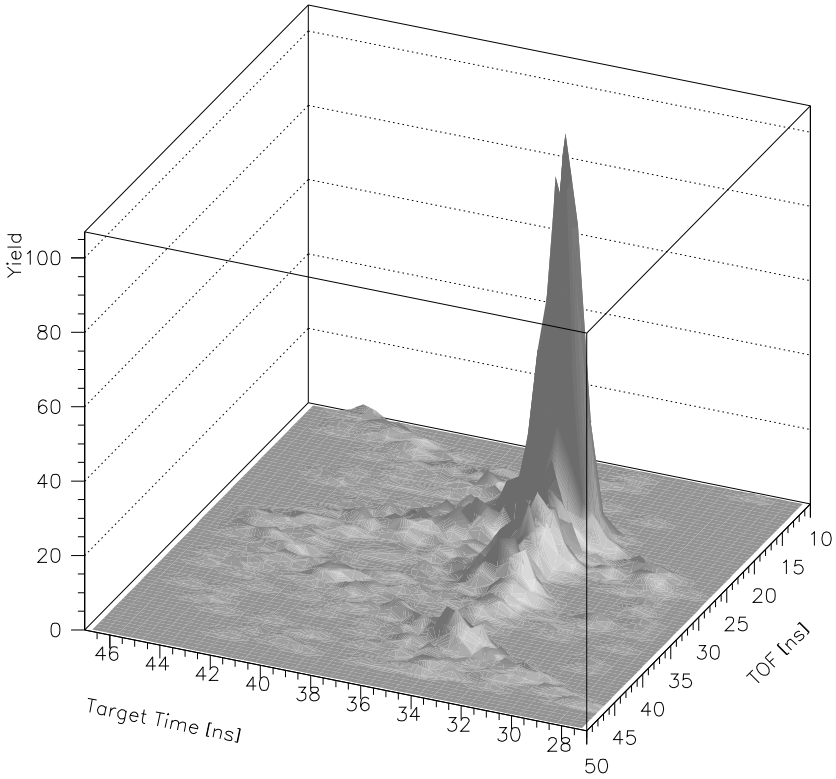


Figure 23: *TOF versus target time with a low energy cut in the target ADC.*

taken, e.g. the dead-time correction asymmetry⁴

$$A_d = \frac{d(1) - d(0)}{d(0) + d(1)}. \quad (67)$$

A_d would be directly the systematic shift in the asymmetry, when ϵ is zero. As can be seen in figure 24, the corrections are in the order of 0.05% per run, but uniformly spread around 0, while the dead-time itself is 2%. The total dead-time asymmetry correction (summed over all runs) for A_{zx} is therefore

⁴The **dead-time** is actually defined as $1 - \frac{t_r}{p_{tr}}$, where the **lifetime** is $\frac{t_r}{p_{tr}}$ and the **dead time correction** 1/lifetime

smaller than 0.01%.

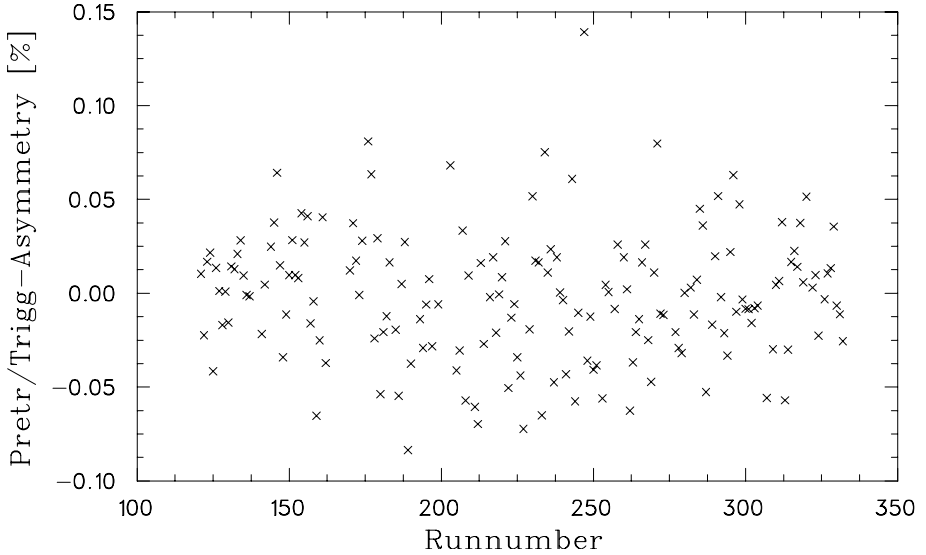


Figure 24: *Pre-trigger to trigger asymmetry in %.*

Although the FC is not very sensitive to small shifts in the beam position, it still could be a candidate for producing false asymmetries when using it for normalization. As can be seen in figure 10 there is an indication that the beam position is slightly different in the horizontal direction, because Na-I detectors show different pulse heights for spin up and spin down. Instead of using the FC for beam current measurement, one can take the single trigger rate of the proton target (ST). Because the target single rate is not too high ($140kHz$), it can be taken for beam current normalization. If the FC would be correct, the relative asymmetry of the ST and the FC ($A_{ST/FC}$) (see equation 68) should be zero.

$$A_{ST/FC} = \frac{\frac{ST(1)}{FC(1)} - \frac{ST(0)}{FC(0)}}{\frac{ST(0)}{FC(0)} + \frac{ST(1)}{FC(1)}} \quad (68)$$

In figure 25 the inverse asymmetry of the FC ($A_{1/FC}$) is plotted as well as $A_{ST/FC}$. $A_{ST/FC}$ is indeed not zero. While the FC seems to be not sensitive to the change of the solenoid field, the ST (resp. ST/FC) shows a stronger dependence.

$A_{ST/FC}$ gives a direct measure for the false asymmetry, when using the FC for normalization: The systematic effect would be in the order of 0.6%, while the beam current correction itself is in the order of 1%.

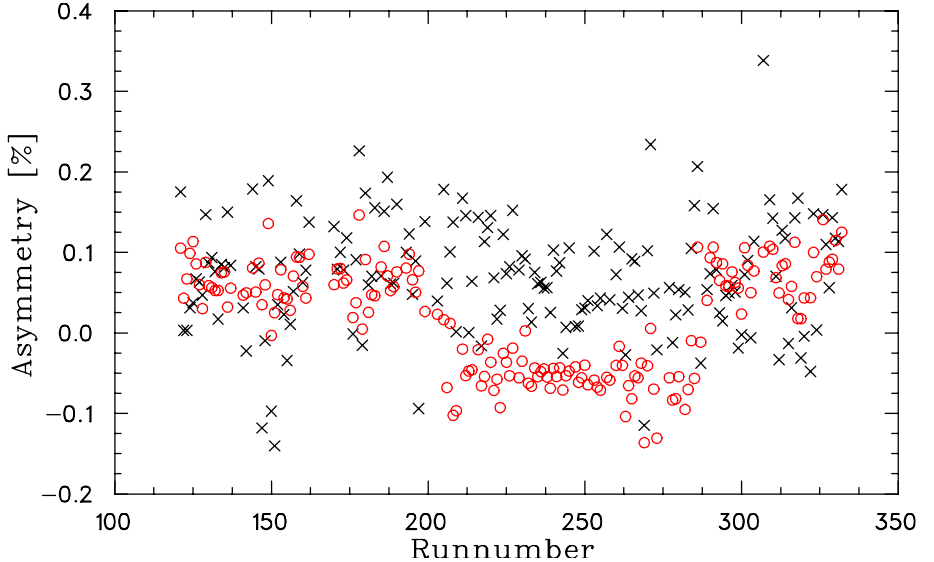


Figure 25: *FC asymmetry (black crosses) and $A_{ST/FC}$ (red circles) as a function of the run number.*

A further check for false asymmetries can be made using the background (see figure 20 (1) and (2)), which should not depend on the polarization of the neutron.

Another possibility is the coincident “background” from the carbon reactions. The scattering process $^{12}\text{C}(\vec{n}, np)$ is also independent of the neutron polarization (at least with the present polarizations in z-direction). In figure 26 the asymmetries from the areas (1), (2) and from the carbon background (5) are summarized with the corrections from above. The asymmetries are zero within the errors. When there is a small overall asymmetry, it is negative, which can be understood from the trigger setup: Because the neutron detector registers neutrons with a much lower single trigger rate than the target, it happens that an elastic neutron from the desired reaction is in coincidence with the background from the target. Of course it is also possible to have a good target proton event with background in the neutron detector from another bunch (2). From all the uncorrelated background, these events would produce an asymmetry due to the main n-p reaction.

4.8 The Carbon Background

The coincident background in figure 20 (5) is mainly resulting from neutron scattering on ^{12}C . Elastic scattering off carbon is not detected, because the

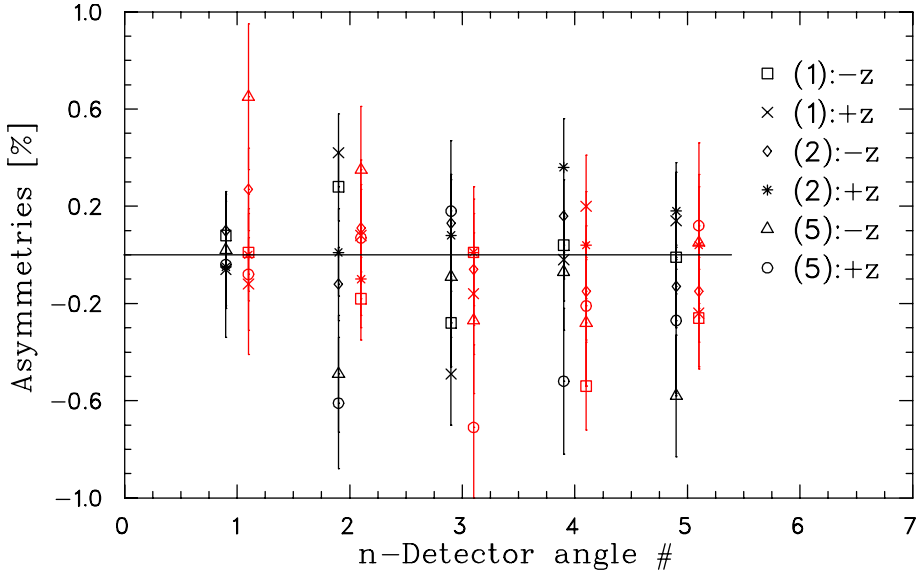


Figure 26: *Asymmetry from the background: black: A_{zx99} and red: A_{zx2000} as a function of the 5 scattering angles in numbers. For better visibility the red and black points are separated. The labels are from figure 20 and z ($-z$) indicates the direction of the solenoid.*

recoil carbon has an energy of about 1.5 MeV which is undetectable due to the strong reduction in the light output of heavier particles [34].

The background must result from inelastic scattering. There are not many scattering data available at such low energies. Especially not differential cross section data. One can get a rough idea of the cross sections from [30,35], where the different channels are studied in detail. Best detected in the scintillating recoil detector are protons, all other particles need much more energy to be detected. The best candidate is the reaction: $^{12}\text{C}(n, n'p)^{11}\text{B}$ with a total cross section of about 90 mb at an energy of 90 MeV, which is not too far from what one would infer from this experiment. The neutron energies from other reactions like $^{12}\text{C}(n, n'3\alpha)$ are similar to inelastic scattering with the corresponding Q -value, because the reaction is assumed to be indirect.

Assuming that $^{12}\text{C}(n, n'p)^{11}\text{B}$ is a quasi free reaction the kinematics of the scattering process can be calculated. In figure 27 the TOF of the fastest neutrons without any restrictions in the recoil proton angle is shown. For comparison the solid line shows the TOF for the slowest neutrons from the main $H(n, np)$ -reaction, which have a flight time of 22.4 ns taking the mean incident neutron energy of 66.24 MeV.

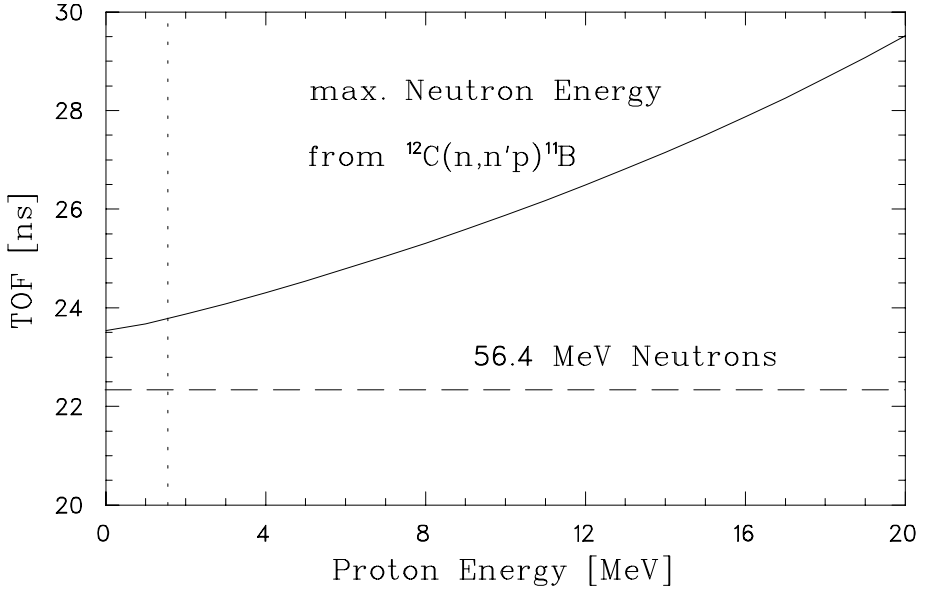


Figure 27: Reaction on ^{12}C . The dashed vertical line corresponds to the threshold for detecting protons. The solid line represents the slowest neutrons from the $H(n, np)$ -reaction for the mean incident neutron energy. The scattered neutrons have an energy of 56.4 MeV corresponding to a flight time of 22.4 ns. The solid line shows the maximal neutron energy from a 3 body calculation of the reaction $^{12}\text{C}(n, n')^{11}\text{B}$.

In all other bars the $H(n, np)$ -reaction has faster neutrons. For this extreme case, the difference in the neutron flight times is 1.8 ns. This difference would be too small to be resolved within the timing resolution of the neutron TOF. For small neutron angles the energy of the proton is smallest which would cause a problem. Fortunately the neutron energies are largest and therefore the TOF is smallest at these angles. For the higher angles, the neutron energy is small, but on the other hand the energy of the protons is higher (see figure 22). In figure 28 the TOF as a function of the proton energies is plotted for both the neutrons scattering off carbon (as in figure 27) and the neutrons from elastic proton scattering. The time difference is more or less constant over the angular region of the neutron detector and it has a value of nearly 3 ns. Experimentally there is a carbon bump visible about 4 ns separated from the elastic peak in figure 29. Not all the background can be excluded, but by using a cut of width 3 ns on the main TOF peak one can get rid of most of it. The rest has to be treated as a systematic uncertainty. The dependence on the cut width in the TOF amounts to 0.4% for the neutrons scattered at 35.32° to 45.68° , 0.6% for

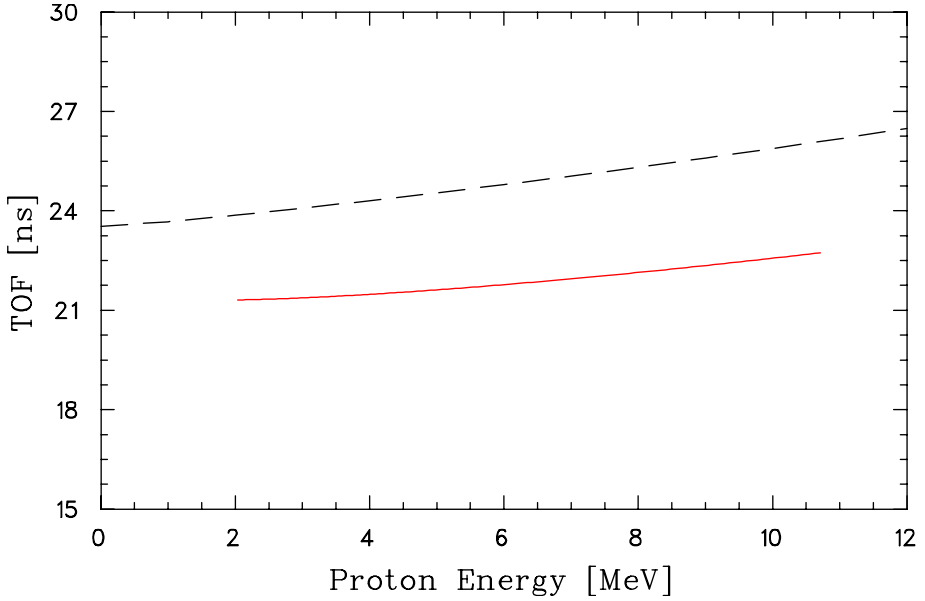


Figure 28: *TOF for neutron-carbon scattering (black dashed line) and for n-p scattering (red solid line).*

the 30.6° CM scattering angle and 1% for the smallest scattering angle, when not going further than 3 ns. This is acceptable given the contribution of other systematic errors.

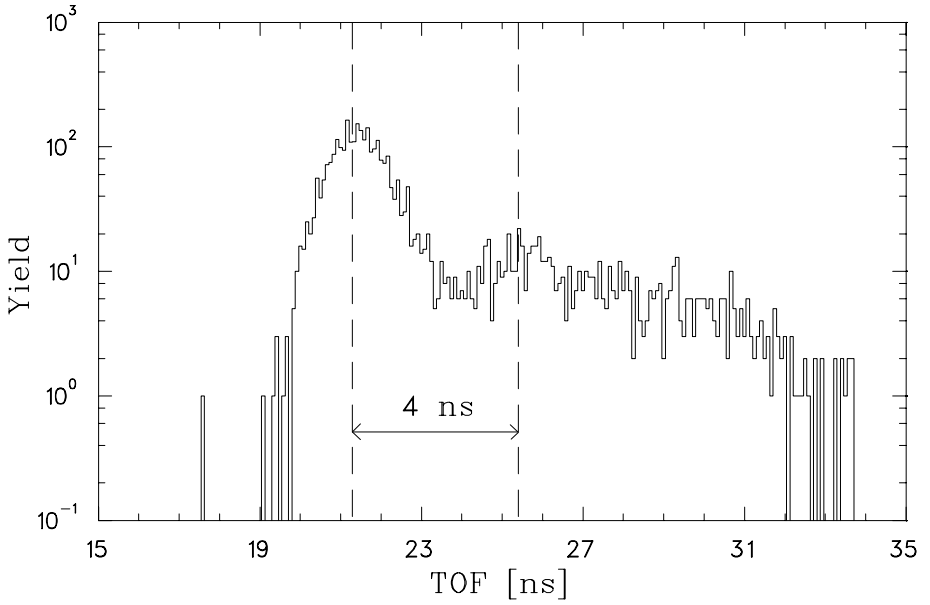


Figure 29: n - p elastic peak and carbon background. The peak with 4 ns time difference is assumed to originate from $^{12}\text{C}(n, n'p)^{11}\text{B}$.

5 Results

With equation 39, the weighted polarization \vec{P}_b from equation 63, the beam current and dead time corrections discussed in chapter 4.7, A_{zx} can finally be calculated from the data:

$$A_{zx} = \frac{1}{a_6 + a_7} (\epsilon_{\pm} - a_2 A_y - a_3 A_{xx} - a_4 A_{yy} - a_5 A_{zz}) \quad (69)$$

$$\epsilon_{\pm} = \frac{d\sigma^{\uparrow} - d\sigma^{\downarrow}}{2 d\sigma_0} \quad (70)$$

$$d\sigma_0 = 1/2 \frac{d\sigma^{\uparrow} + d\sigma^{\downarrow}}{1 \mp a_1 A_y}. \quad (71)$$

The factors $a_1 \dots a_7$ are (see equations 32-38):

$$a_1 = \mp \cos(\vartheta) \langle \sin(\phi) \rangle_{\theta} |P_t| \quad (72)$$

$$a_2 = \langle \sin(\phi) \rangle_{\theta} |P_b^x| \mp \langle \cos(\phi) \rangle_{\theta} |P_b^y| \quad (73)$$

$$a_3 = \pm \cos(\vartheta) |P_t| (-\langle \cos^2(\phi) \rangle_{\theta} |P_b^x| \mp \langle \cos(\phi) \sin(\phi) \rangle_{\theta} |P_b^y|) \quad (74)$$

$$a_4 = \cos(\vartheta) \langle \sin(\phi) \cos(\phi) \rangle_{\theta} |P_b^y P_t| \quad (75)$$

$$a_5 = \mp \sin(\vartheta) |P_b^z P_t| \quad (76)$$

$$a_6 = \pm \cos(\vartheta) \langle \cos(\phi) \rangle_{\theta} |P_b^z P_t| \quad (77)$$

$$a_7 = \sin(\vartheta) |P_t| (\pm \langle \cos(\phi) \rangle_{\theta} |P_b^x| + \langle \sin(\phi) \rangle_{\theta} |P_b^y|). \quad (78)$$

The beam polarization in x-direction $|P_b^x|$ for a 3 ns target time cut is given by $|P_b^x| = 0.0002 \cdot |P_b^z|$. This allows to neglect all terms with P_x for cuts around 3 ns. A_{xx} , A_{yy} , A_{zz} and A_y with their errors are shown in table 5. The uncertainties in the correlation parameters result from a $\pm 1^\circ$ -variation for ϵ_1 (taken from a PSA in [9]). The values for A_y are from a measurement of our group published in [36]. The resulting values for A_{zx} are the mean for

CM-angle [$^\circ$]	A_y	A_{xx}	A_{yy}	A_{zz}	$ \epsilon_{\pm} $
25.32 $^\circ$	0.161(11)	0.19(2)	0.41(3)	0.18(8)	0.01304(16)
30.67 $^\circ$	0.194(11)	0.16(2)	0.44(3)	0.16(8)	0.01563(12)
35.82 $^\circ$	0.223(11)	0.14(2)	0.47(3)	0.14(8)	0.01465(13)
41.00 $^\circ$	0.250(11)	0.12(2)	0.49(3)	0.12(8)	0.01891(12)
45.68 $^\circ$	0.270(11)	0.11(2)	0.51(3)	0.09(8)	0.02032(13)

Table 5: A_y , A_{xx} , A_{yy} , A_{zz} and $|\epsilon_{\pm}|$. The numbers in brackets are the errors of the last digits. $|\epsilon_{\pm}|$ is the absolute mean taken over the possible target field and Solenoid field settings.

different TOF cuts up to 3 ns and different cuts around 3 ns for the target

time which corresponds to a neutron mean energy of 66.24 MeV. The terms ϵ_{\pm} and $a_1 \cdots a_7$, which depend on the polarizations are presented in table 9 in appendix D.

Obviously, the most important corrections to the measured asymmetry ϵ_{\pm} are $a_2 A_y$ and $a_5 A_{zz}$, the former in the order of 0.12, the latter 0.04. They give both a positive correction, independently of the target polarization. The next lower correction is $a_4 A_{yy}$ in the order of 0.01. It contributes either negatively for positive target polarization or positively for negative target polarization. The other terms are smaller than 0.01.

The final values for A_{zx} with the different target polarization directions and solenoid field settings are shown in table 6. The final values for each angle, i.e.

	$A_{zx}(++)$	$A_{zx}(-+)$	$A_{zx}(+-)$	$A_{zx}(--)$
P_b^x	0.02	0.02	0.00	0.00
P_b^y	9.54	9.47	9.18	9.05
P_b^z	26.44	27.23	25.44	25.08
P_t	55.14	58.96	67.50	68.50
25.32°	0.045(25)	0.038(24)	0.049(22)	0.055(17)
30.67°	0.035(18)	0.042(17)	0.059(13)	0.053(14)
35.82°	0.083(18)	0.063(18)	0.070(14)	0.059(17)
41.00°	0.054(16)	0.056(18)	0.043(14)	0.057(18)
45.68°	0.065(17)	0.042(20)	0.047(15)	0.041(19)

Table 6: Beam (P_b) and target (P_t) polarizations and A_{zx} for different settings of the solenoid and the target polarization as a function of the target angles: (+ -): Solenoid $+\vec{e}_z$ and target $-\vec{e}_x$. The brackets are the errors of the two last digits.

the mean values from table 6, are given in table 7: The statistical error $\Delta_{stat}A_{zx}$

CM-angle [$^\circ$]	A_{zx}	Δ_{stat}	Δ_{sys}
25.32°	0.048	0.011	0.019
30.67°	0.049	0.008	0.019
35.82°	0.068	0.008	0.019
41.00°	0.051	0.008	0.019
45.68°	0.050	0.009	0.019

Table 7: A_{zx} at 66.24 MeV with the statistical error Δ_{stat} and systematic error Δ_{sys} .

is the uncertainty due to the number of counts. All other uncertainties arising

from the corrections of A_y , A_{xx} , A_{yy} and A_{zz} as well as the polarization errors are taken into the systematic error $\Delta_{sys}A_{zx}$.

All systematic effects and their consequences for the total systematic error of A_{zx} are listed in table 8. A_{zz} has the biggest uncertainty. Since A_{zz} has been

	<i>Error</i>	$\Delta_{sys}A_{zx}$
ΔA_{zz}	0.08	0.017
ΔA_y	0.01	0.007
ΔP_t	0.02	0.004
ΔP_b	0.003	0.002
ΔA_{yy}	0.02	0.0007
ΔA_{xx}	0.02	0.0005
Total	-	0.019

Table 8: *Systematic uncertainties*

measured with the same setup by our group, the uncertainty in this parameter will be less than 0.01 after the data have been analyzed. With that information the systematic error of A_{zx} can be significantly reduced .

The energy distribution $n(T)$, with its mean energy of 66.24 MeV, is taken from figure 16. The angle distributions, which give the 5 mean angles, are shown in figure 32.

6 Discussion

As a comparison with a phase shift analysis from SAID, figure 30 shows the data and the A_{zx} values calculated with different values of the phase ϵ_1 . They seem to match better with a lower value of ϵ_1 . It would be an indication for a tensor force as predicted from the potentials but in disagreement with the PSA of Henneck [5].

On the other hand it is dangerous to derive conclusions directly from such a comparison. It is necessary to perform a PSA with the available data including the present work and the A_{zz} , because the fitting must be done for all phases and mixing parameters. The more data there are in the database for a PSA, the more accurate the results for ϵ_1 . The fit to the phases and mixing parameters within a PSA has to be derived from fitting angle and energy dependences simultaneously.

Especially the energy dependence causes problems in drawing a conclusion. A_{zx} is very sensitive to the energy as can be seen in figure 31. But obviously the data base has no data between 50 and 75 MeV, which manifests itself in a straight line between these energies. The functional dependence on the energy is therefore not clear.

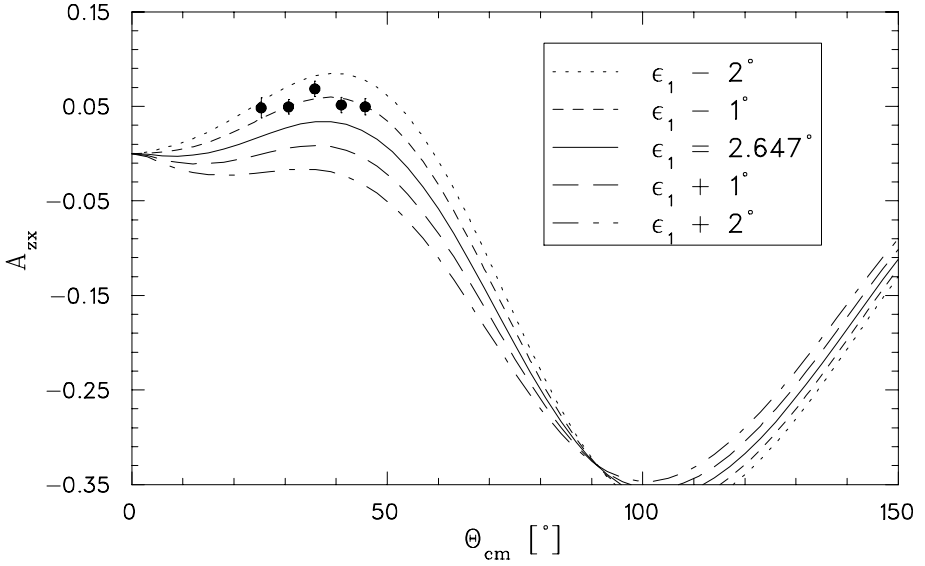


Figure 30: *The present A_{zx} -data (\circ) and the statistical error as a function of the CM-angle with different PSA interpolated values for ϵ_1*

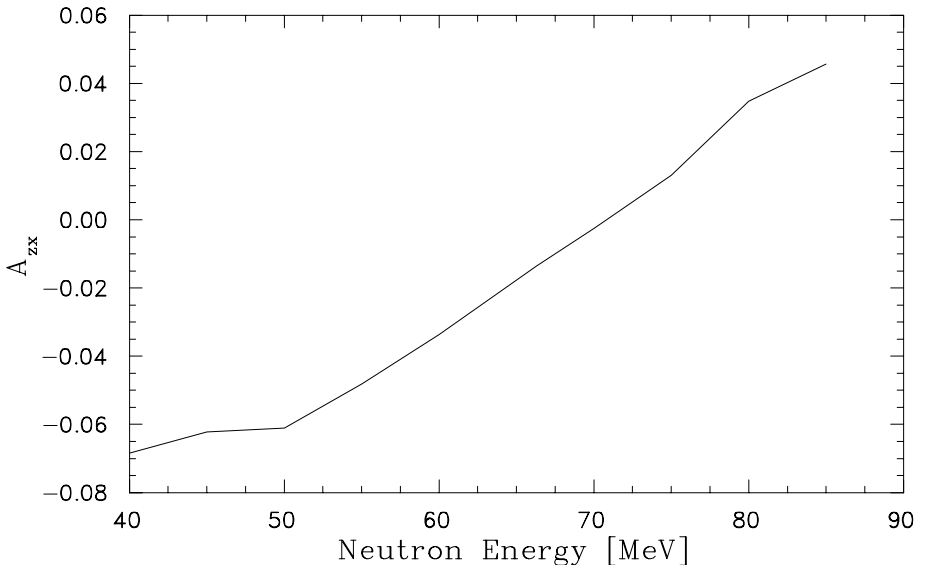


Figure 31: *A_{zx} as a function of the energy. The squares are interpolated points from a phase shift analysis from the online analysis program SAID [10] for a fixed CM angle of 36°*

In a recent PSA from D. Arndt [37], he claims that there are no discrepancies seen between his PSA and the potential calculations, but no data were in the data-base between 50 and 80 MeV. On the other hand the PSA of D. Henneck [5] (see figure 2) shows higher values.

7 Conclusion

The goal of this work is to contribute to an accurate determination of the phases and mixing parameters in the energy region below 100 MeV. Especially the lack of data between 50 and 75 MeV was problematic and has been improved with the present measurements.

We expect that this work will significantly reduce the uncertainties of the phases, when a new global PSA is performed, and help to find a more accurate answer to the strength of the tensor force in the NN-interaction.

A Neutron Spin Rotation in the FC-Magnetic Field

In the reaction $D(\vec{p}, \vec{n})pp$ at zero degrees the neutrons have a broad momentum distribution, even if the initial proton is monoenergetic. The reason lies in the three body nature of the breakup reaction of the deuteron-proton system. The distribution $n(k_i)$ is known as well as the polarization distribution of the neutrons directly after scattering. The neutrons pass the FC-magnet where their polarization is turned from \vec{e}_x into \vec{e}_z . But the time Δt during which the neutrons are in the magnetic field is obviously depending on their initial momenta and therefore the spin is differently turned for each momentum k_i . This can also produce a non zero polarization in \vec{e}_x and $-\vec{e}_x$ direction, respectively. The spin rotation in the magnetic field will be treated non-relativistically.

Because the FC magnetic field B_{FC} is oriented in $+\vec{e}_y$ the Hamiltonian for the neutrons is:

$$H = H_o - g_n \mu_k \vec{S} \cdot \vec{B} = H_o - g_n \mu_k S_y B_y \quad (79)$$

$$= \frac{k^2}{2m} - 1/2 g_n \mu_k \begin{pmatrix} 0 & -i \\ i & 0 \end{pmatrix} \quad (80)$$

The neutrons are either polarized in $+\vec{e}_x$ or $-\vec{e}_x$. Without loss of generality the beam density can be replaced by an eigenstate of the spin operator S_x which signifies that the beam is polarized to 100%. Initially unpolarized neutrons stay unpolarized passing the magnet.

With

$$S_x = \frac{1}{2} \begin{pmatrix} 0 & 1 \\ 1 & 0 \end{pmatrix} \quad (81)$$

the spin operator in x -direction and assuming that the neutron is in a space eigenstate of H_o in front of the magnet (at time t_0) the eigenstates are:

$$|\psi(t_0)\rangle = \frac{1}{\sqrt{2}} \begin{pmatrix} e^{ik_z \cdot z} \\ e^{ik_z \cdot z} \end{pmatrix} \text{ for positive } (+\vec{e}_x) \text{ polarization} \quad (82)$$

$$|\psi(t_0)\rangle = \frac{1}{\sqrt{2}} \begin{pmatrix} e^{ik_z \cdot z} \\ -e^{ik_z \cdot z} \end{pmatrix} \text{ for negative } (-\vec{e}_x) \text{ polarization.} \quad (83)$$

The passage through the magnet is a time translation with the full Hamiltonian H described by the time translation operator $U(\Delta t)$, where $\Delta t = t - t_o$:

$$U(\Delta t) = \exp(-i/\hbar H \cdot (\Delta t)) \quad (84)$$

$$\begin{aligned} &\hat{=} \exp(-i/\hbar \frac{k^2}{2m} \cdot (\Delta t)) \cdot \\ &\exp(\frac{i}{2\hbar} g_n \mu_k B_y \cdot \Delta t \begin{pmatrix} 0 & -i \\ i & 0 \end{pmatrix}) \end{aligned} \quad (85)$$

The propagated state $|\psi(t)\rangle$ in the magnetic field is simply:

$$\begin{aligned} |\psi(t)\rangle_{\pm} &= U(\Delta t) |\psi(t_0)\rangle \\ &= \frac{1}{\sqrt{2}} \exp\left(\begin{pmatrix} 0 & \frac{1}{2\hbar} g_n \mu_k B_y \cdot (\Delta t) \\ -\frac{1}{2\hbar} g_n \mu_k B_y \cdot (\Delta t) & 0 \end{pmatrix} \right) \\ &\times \begin{pmatrix} \exp(i p \cdot z - i/\hbar k^2/2m \Delta t) \\ \pm \exp(i p \cdot z - i/\hbar k^2/2m \Delta t) \end{pmatrix} \end{aligned} \quad (86)$$

$$\begin{aligned} &= \frac{1}{\sqrt{2}} \begin{pmatrix} \cos(\Lambda) & \sin(\Lambda) \\ -\sin(\Lambda) & \cos(\Lambda) \end{pmatrix} \\ &\times \begin{pmatrix} \exp(i p \cdot z - i/\hbar k^2/2m \Delta t) \\ \pm \exp(i p \cdot z - i/\hbar k^2/2m \Delta t) \end{pmatrix} \end{aligned} \quad (87)$$

$$\Lambda = \frac{1}{2\hbar} g_n \mu_k B_y \Delta t. \quad (88)$$

The + sign in equation 87 is for positive ($+\vec{e}_x$) and - for ($-\vec{e}_x$) neutron polarizations. With $\phi_0(\Delta t) = 1/\sqrt{2} \exp[ipz - i/(\hbar 2m) p^2 \Delta t]$ the propagated states can be written as:

$$|\Psi(t)\rangle_+ = \phi_0(\Delta t) \begin{pmatrix} \cos \Lambda + \sin \Lambda \\ \cos \Lambda - \sin \Lambda \end{pmatrix} \quad (89)$$

$$|\Psi(t)\rangle_- = \phi_0(\Delta t) \begin{pmatrix} \cos \Lambda - \sin \Lambda \\ -\cos \Lambda - \sin \Lambda \end{pmatrix} \quad (90)$$

The polarization of the neutrons and the beam, respectively, at time t for initially in $+\vec{e}_x$ polarized and in $-\vec{e}_x$ polarized particles ($\vec{P}_{\pm}(t)$) is

$$\vec{P}_+(t) = \begin{pmatrix} \cos^2 \Lambda - \sin^2 \Lambda \\ 0 \\ 2 \sin \Lambda \cos \Lambda \end{pmatrix} \quad (91)$$

$$\vec{P}_-(t) = - \begin{pmatrix} \cos^2 \Lambda - \sin^2 \Lambda \\ 0 \\ 2 \sin \Lambda \cos \Lambda \end{pmatrix}. \quad (92)$$

From equations 91 and 92 it can be seen that in the ideal case where $|\Lambda| = \Pi/4$, the polarization is turned simply from x to $-z$ or from $-x$ to z . Note that g_n is negative!

B Neutron Spin Rotation in the Target Field

The calculation of the spin rotation in the target magnetic field doesn't even allow to use a perturbative approach, because of high gradients near the target. The problem can be solved by numerical integration of the Schrödinger's equation. The integration is practicable with limited computer resources, but high accuracy.

The target field is rotationally symmetric around the x-axis and has therefore no y-component. With t_o the time after the FC field and t_t the time at the target, the problem to solve is simply:

$$\int_{t_o}^{t_t} \frac{d}{dt} |\psi(t)\rangle dt = \int_{t_o}^{t_t} -\frac{i}{\hbar} H |\psi(t)\rangle dt \quad (93)$$

$$H = -g_n \mu_k (S_x B_x(t) + S_z B_z(t)) \quad (94)$$

$$\hat{=} -\frac{i g_n \mu_k}{2 \hbar} \begin{pmatrix} B_z(t) & B_x(t) \\ B_x(t) & -B_z(t) \end{pmatrix}. \quad (95)$$

The time t as a function of the distance z from the target can be calculated from equation 60 (for a given energy T). The first integration step, which is the state after the time dt : $|\psi(dt)\rangle$. The ground state ($t_o = 0$) shall be the spin state after the FC field (see equations 89 and 90):

$$\begin{aligned} |\psi(dt)\rangle_{\pm} &\hat{=} \begin{pmatrix} \psi_{\pm}^{\uparrow}(dt) \\ \psi_{\pm}^{\downarrow}(dt) \end{pmatrix} \quad (96) \\ &= \frac{1}{\sqrt{2}} \begin{pmatrix} \cos \Lambda \pm \sin \Lambda \\ \pm \cos \Lambda - \sin \Lambda \end{pmatrix} + \frac{1}{\sqrt{2}} \frac{i g_n \mu_k}{2 \hbar} \\ &\cdot \begin{pmatrix} B_z(dt) & B_x(dt) \\ B_x(dt) & -B_z(dt) \end{pmatrix} \begin{pmatrix} \cos \Lambda \pm \sin \Lambda \\ \pm \cos \Lambda - \sin \Lambda \end{pmatrix} dt. \quad (97) \end{aligned}$$

The upper sign is for initially in $+\vec{e}_x$, the lower for $-\vec{e}_x$ polarized neutrons (before the FC-field).

The state after the time $n \cdot dt$ is recursively calculated from the state at time $(n-1) \cdot dt$:

$$\begin{aligned} \begin{pmatrix} \psi_{\pm}^{\uparrow}(n \cdot dt) \\ \psi_{\pm}^{\downarrow}(n \cdot dt) \end{pmatrix} &= \begin{pmatrix} \psi_{\pm}^{\uparrow}((n-1) \cdot dt) \\ \psi_{\pm}^{\downarrow}((n-1) \cdot dt) \end{pmatrix} \quad (98) \\ &+ \frac{i g_n \mu_k}{2 \hbar} \begin{pmatrix} B_z(n \cdot dt) & B_x(n \cdot dt) \\ B_x(n \cdot dt) & -B_z(n \cdot dt) \end{pmatrix} \\ &\times \begin{pmatrix} \psi_{\pm}^{\uparrow}((n-1) \cdot dt) \\ \psi_{\pm}^{\downarrow}((n-1) \cdot dt) \end{pmatrix} dt. \quad (99) \end{aligned}$$

C Error Calculations

The statistical error for all yields (N) in the experiment is obtained from:

$$\Delta N = \sqrt{N} \quad (100)$$

The values taken from the scalers like beam current, trigger and pre-trigger counts are assumed to have no error, since the corresponding numbers are very large.

The uncertainties for derived quantities are calculated from the first Taylor expansion in each variable to get the usual error propagation (see [38]):

$$\Delta f(x_1, \dots, x_n) = \sqrt{\sum_{i=1}^n \left(\frac{\partial}{\partial x_i} f(x_1, \dots, x_n) \Delta x_i \right)^2}, \quad (101)$$

for an arbitrary function f which depends on the variables x_1, \dots, x_n .

The distributions of the scattering angles $dn(\theta(x_n, y_n, z_n))/d\theta$, which depend on the coordinates of the neutron detector (x_n, y_n, z_n) are shown in figure 32 as a function of the lab angle. The energy distribution of the incident

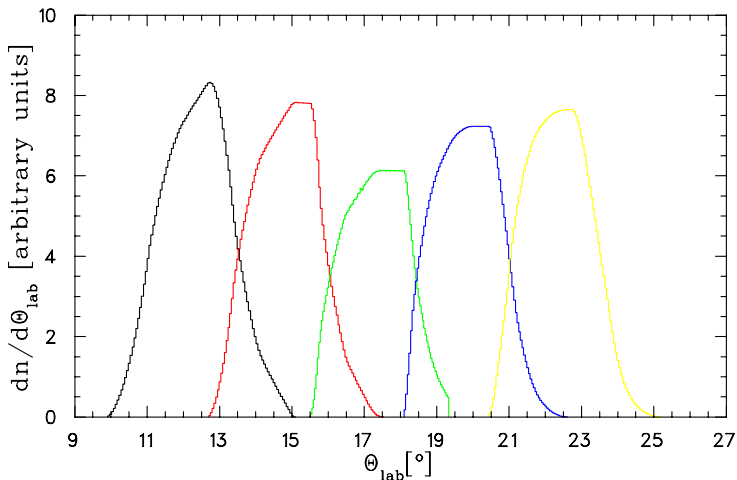


Figure 32: *Distribution of the scattering angle θ in the lab frame for the 5 mean angles: 12.41 black, 15.03° red, 17.56° green, 20.10° blue, 22.41° yellow*

neutrons is taken from the energy distribution presented in figure 16 for a 3 ns cut in the target time.

The energy- as well as the angular distributions can be taken into account in a new PSA-fit.

D Asymmetry and Correction Factors

In the following table the measured asymmetry ϵ_{\pm} and the correction factors of equation 71 are presented for the two settings of the Solenoid field direction and the target polarizations.

	(++)	(-+)	(+-)	(--)
ϵ_{\pm}	-0.0130(25)	-0.0137(34)	0.0135(35)	0.0124(27)
	-0.0170(26)	-0.0158(26)	0.0147(22)	0.0154(23)
	-0.0125(26)	-0.0149(27)	0.0149(23)	0.0164(27)
	-0.0183(22)	-0.0176(27)	0.0208(23)	0.0183(29)
	-0.0181(24)	-0.0208(29)	0.0213(24)	0.0219(31)
a_1	-0.0075	-0.0080	0.0092	0.0093
	-0.0078	-0.0083	0.0095	0.0097
	-0.0078	-0.0084	0.0096	0.0097
	-0.0077	-0.0083	0.0095	0.0096
	-0.0075	-0.0080	0.0091	0.0093
a_2	-0.0910	-0.0903	0.0875	0.0862
	-0.0925	-0.0917	0.0889	0.0876
	-0.0933	-0.0926	0.0897	0.0884
	-0.0939	-0.0903	0.0902	0.0890
	-0.0942	-0.0917	0.0897	0.0892
a_3	-0.0040	-0.0042	-0.0045	-0.0045
	-0.0036	-0.0038	-0.0041	-0.0041
	-0.0032	-0.0034	-0.0036	-0.0036
	-0.0029	-0.0031	-0.0033	-0.0033
	-0.0026	-0.0028	-0.0036	-0.0030
a_4	0.0039	0.0041	0.0046	0.0046
	0.0035	0.0037	0.0041	0.0041
	0.0031	0.0033	0.0037	0.0037
	0.0028	0.0030	0.0033	0.0033
	0.0025	0.0027	0.0037	0.0030
a_5	-0.0303	-0.0322	0.0357	0.0357
	-0.0303	-0.0322	0.0357	0.0357
	-0.0303	-0.0322	0.0357	0.0357
	-0.0303	-0.0322	0.0357	0.0357
	-0.0303	-0.0322	0.0357	0.0357

a_6	0.1360	0.1443	-0.1602	-0.1603
	0.1382	0.1465	-0.1627	-0.1628
	0.1394	0.1479	-0.1642	-0.1643
	0.1403	0.1488	-0.1652	-0.1653
	0.1407	0.1492	-0.1642	-0.1658
a_7	0.0010	0.0010	0.0011	0.0011
	0.0008	0.0009	0.0010	0.0010
	0.0007	0.0008	0.0008	0.0008
	0.0006	0.0007	0.0007	0.0007
	0.0006	0.0006	0.0008	0.0007

Table 9: Measured asymmetries ϵ_{\pm} and correction factors $a_1 \cdots a_7$ of equation 71 for all 5 angles (the lowest angle is always on top). The settings of the Solenoid field and the target polarization are indicated by the \pm signs; e.g. (+ -): Solenoid $+\vec{e}_z$ and target $-\vec{e}_x$.

References

- [1] R. Machleidt. *Adv. in Nucl. Phys.*, 19:189, 1989.
- [2] J.Schwinger. *Phys. Rev.*, 55:235, 1939.
- [3] H.A.Bethe. *Phys. Rev.*, 57:728, 1940.
- [4] S. Ishikawa and T. Sasakawa. *Phys. Rev. C*, 36:2037, 1987.
- [5] R. Henneck. *Phys. Rev. C.*, 47:1859, 1993.
- [6] H. Arenhoevel. *Prog. Th.Phys.Suppl.*, 91:1, 1987.
- [7] J.J.Sakurai. *Modern Quantum Mechanics, Addison-Wesley*, 1994.
- [8] H.P.Stapp, T.J.Ypsilantis, and N.Metropolis. *Phys. Rev.*, 105:302, 1957.
- [9] R.A. Arndt, J.S. Hyslop, and L.D. Roper. *Phys. Rev. D*, 35:128, 1987.
- [10] R.A. Arndt. 1995. Program SAID, available from R.A. Arndt and L.D. Roper.
- [11] W.N. Cottingham, M. Lacombe, B. Loiseau, J.M. Richard, and R. VinhMau. *Phys. Rev. D*, 8:800, 1973.
- [12] R.A. Arndt et al. *Phys. Rev. D*, 45:3995, 1992.
- [13] M.M. Nagels, T.A. Rijken, and J.J. de Swart. *Phys. Rev. D*, 17:768, 1978.
- [14] G.G. Ohlsen. Polarization transfer and spin correlation experiments in nuclear physics. *Rep. Prog. Phys.*, 35:771, 1972.
- [15] M. Simonius. Theory of polarization measurements, observables, amplitudes and symmetries. *Lecture Notes in Physics, Polarization Nuclear Physics*, 30:38, 1973.
- [16] Basle convention. *Nucl. Phys.*, 21:696, 1960.
- [17] H.H. Barschall and W. Haeberli (editors). *University of Wisconsin Press*, page 25, 1971.
- [18] J. Bystricky, F. Lehar, and P.Winternitz. *Jour. de Phys.*, 39:1, 1978.
- [19] L. Wolfenstein and J. Ashkin. *Phys. Rev.*, 85:947, 1952.
- [20] L. Wolfenstein. *Phys. Rev.*, 96:1654, 1954.
- [21] J.M. Blatt and V. Weisskopf. *Theoretical Nuclear Physics, John Wiley and Sons Inc., New York*, 1952.

- [22] J.M. Blatt and L.C. Biedenharn. *Phys. Rev.*, 86:399, 1952.
- [23] P.A. Schmelzbach. Ecr-ionizer for intense polarized beams. Proc. of Int. workshop on Polarized Ion Sources and Polarized Gas Jets KEK Tsakuba, 1990.
- [24] B. Zihlmann. PhD thesis, University of Basel, 1995.
- [25] P. Haffter. *The Spin-Dependent Total Cross Section $\Delta\sigma_L$ In N-P Scattering At 66.2 MeV*. PhD thesis, University of Basel, 1991.
- [26] R. Henneck, C. Gysin, M. Hammans, J. Jourdan, W. Lorenzon, M.A. Pickar, I. Sick, S. Burzynski, and T. Stammach. *Nucl. Instr. Meth. A*, 259:329, 1987.
- [27] B. van den Brandt, E.I. Bunyatova, P. Hautle, J.A. Konter, and S. Mango. *PSI Newsletter*, page p12, 1994.
- [28] B. van den Brandt, E.I. Bunyatova, P. Hautle, J.A. Konter, and S. Mango. *Nucl. Instr. and Meth. A*, 356:36, 1995.
- [29] D. Rohe. PhD thesis, University of Mainz, 1998.
- [30] D.A. Kellogg. *Phys. Rev.*, 90:224, 1953.
- [31] P.D. Eversheim, F. Hinterberger, U. Lahr, B. v.Przewoski, J. Campbell, J. Goetz, M. Hammans, R. Henneck, G. Masson, and I. Sick. *Phys. Lett. B*, 234:253, 1990.
- [32] T. Mayer-Kuckuk. *Kernphysik, B.G. Teubner, Stuttgart*, page 172, 1992.
- [33] M. Zeier, H. Anklin, S. Buttazoni, W. Glöckle, A. Honegger, J. Jourdan, H. Mühry, Th. Petitjean, I. Sick, A. Witala, and B. Zihlmann. *Nucl. Phys. A*, 654:541, 1999.
- [34] G.F. Knoll. *Radiation Detection and Measurement, John Wiley and Sons Inc., New York*, 1979.
- [35] A. Del Guerra. *NIM*, 135:337, 1976.
- [36] C. Brogli-Gysin, S. Burzynski, J. Campbell, P. Haffter, M. Hammans, R. Henneck, J.Jourdan, G. Masson, M.A. Pickar, and I. Sick. *Nucl. Phys. A*, 541:137, 1992.
- [37] R.A. Arndt, I. Strakovsky, and R.I. Workman. *Phys. Rev. C*, 62:03005, 2000.
- [38] P.R. Bevington and D. Keith Robinson. *Data Reduction And Error Analysis In The Physical Sciences (Second Edition), McGraw-Hill, Inc., New York*, 1992.

CURRICULUM VITAE

Personalien:

Name: Markus Hauger,
geboren von Liliane und Otto Hauger

Geburt: 29. August 1969 in Basel

Nationalität: Schweiz

Heimatort: Basel

Zivilstand: ledig

Ausbildung:

1977 - 1982 Primarschule in Muttenz (BL)

1982 - 1990 Gymnasium in Basel
22. Juni 1990: Matura Typus B

1990 - 1995 Studium der Physik an der Universität Basel
mit Nebenfach Chemie
29. Oktober 1995: Diplom in Experimentalphysik

1996 - 2001 Promotion in Experimentalphysik im Departement
für Physik und Astronomie der Universität Basel,
ausgebildet von folgende DozentInnen:

G. Backenstoss, G. Baur, J. Fünfschilling, H.-J. Güntherrodt,
H.Ch. Im Hof, J. Jourdan, H.-P. Kraft, P. Oelhafen, H. Rudin,
B. Scarpellini, P. Schiess, I. Sick, P. Talkner, L. Tauscher,
H. Thomas, D. Trautmann, I. Tschokke, Ch. Ullrich, D. Vossiek,
R. Wagner, A.D. Zuberbühler

Forschungs- und Lehrtätigkeiten:

1993 - 1996 Hilfsassistent im Anfängerpraktikum des Instituts für
Physik der Universität Basel

1996 - 2001 Assistent des Praktikums für Radioaktivitätsmessungen
der Universität Basel

1996 - 2001 Experimente am JLAB, Newport News (USA),
am Mainz Microtron (MAMI) in Mainz (D)
und am Paul Scherrer Institut, Villigen (CH)

